J. Fluid Mech. (2009), *vol.* 640, *pp.* 235–264.
doi:10.1017/S0022112009991339

A numerical study of the relaxation and breakup of an elongated drop in a viscous liquid

SHAOPING QUAN[1]†, DAVID P. SCHMIDT[2], JINSONG HUA[3] AND JING LOU[1]

[1]Institute of High Performance Computing, 1 Fusionopolis Way, #16-16 Connexis, Singapore 138632

[2]Department of Mechanical and Industrial Engineering, The University of Massachusetts at Amherst, 160 Governors Drive, Amherst, MA 01003-2210, USA

[3]Department of Process and Fluid Flow Technology, Institute for Energy Technology, Kjeller NO-2027, Norway

(Received 12 January 2009; revised 21 July 2009; accepted 22 July 2009; first published online 29 October 2009)

The relaxation and breakup of an elongated droplet in a viscous and initially quiescent fluid is studied by solving the full Navier–Stokes equations using a three-dimensional finite volume method coupled with a moving mesh interface tracking (MMIT) scheme to locate the interface. The two fluids are assumed incompressible and immiscible. The interface is represented as a surface triangle mesh with zero thickness that moves with the fluid. Therefore, the jump and continuity conditions across the interface are implemented directly, without any smoothing of the fluid properties. Mesh adaptations on a tetrahedral mesh are employed to permit large deformation and to capture the changing curvature. Mesh separation is implemented to allow pinch-off. The detailed investigations of the relaxation and breakup process are presented in a more general flow regime compared to the previous works by Stone & Leal (*J. Fluid Mech.*, vol. 198, 1989, p. 399) and Tong & Wang (*Phys. Fluids*, vol. 19, 2007, 092101), including the flow field of the both phases. The simulation results reveal that the vortex rings due to the interface motion and the conservation of mass play an important role in the relaxation and pinch-off process. The vortex rings are created and collapsed during the process. The effects of viscosity ratio, density ratio and length ratio on the relaxation and breakup are studied. The simulations indicate that the fluid velocity field and the neck shape are distinctly different for viscosity ratios larger and smaller than $O(1)$, and thus a different end-pinching mechanism is observed for each regime. The length ratio also significantly affects the relaxation process and the velocity distributions, but not the neck shape. The influence of the density ratio on the relaxation and breakup process is minimal. However, the droplet evolution is retarded due to the large density of the suspending flow. The formation of a satellite droplet is observed, and the volume of the satellite droplet depends strongly on the length ratio and the viscosity ratio.

1. Introduction

The breakup and deformation of droplets in a suspending fluid is of great interest and has been studied both experimentally and numerically for decades due to the fundamental importance in nature and in engineering applications, such as raindrops,

† Email address for correspondence: quansp@ihpc.a-star.edu.sg

sprays, inkjet printing, etc. The pioneering work on the deformation and breakup of a droplet was performed by Taylor (1932, 1934). He showed that the deformation of an initially spherical droplet by steady linear flow is governed by the viscosity ratio between the drop phase and the suspending fluid and the capillary number (ratio of the viscous forces to surface tension forces). The breakup of the droplet by shear was also experimentally studied, and a critical capillary number for the onset of the breakup was reported. Rallison (1984) reviewed the work on the deformation of small droplets and bubbles in shear flows.

Stone, Bentley & Leal (1986) examined transient effects on the deformation and breakup of a liquid droplet in another viscous fluid using a computer-controlled four-roll mill. In particular, they investigated the continuous deformation and elongation of a liquid drop in a two-dimensional linear flow. In addition, they studied the relaxation and pinch-off process for the deformed and elongated droplet when the imposed linear flow is abruptly terminated. They showed that the end-pinching (a mechanism proposed by Stone *et al.* 1986 for the breakup of an elongated droplet) has a strong dependence on the viscosity ratio, and specifically, for the viscosity ratio greater than unity, much longer elongation is needed to guarantee breakup. A qualitative explanation of the end-pinching was proposed. In order to further investigate the end-pinching mechanism, a detailed study of the relaxation and breakup of an elongated droplet at low Reynolds numbers was performed by Stone & Leal (1989) using a boundary integral method. Their numerical results indicated that the relaxation and breakup process is totally determined by the viscosity ratio and the initial shape of the elongated droplet. They also proposed that the end-pinching is the competition between a surface tension driven flow near the end and a pressure-driven flow away from the centre of the elongated droplet. It was found that the capillary-wave instability mechanism cannot be used to explain the relaxation and breakup process of a moderately elongated droplet in another fluid. These numerical simulations were limited to low-Reynolds-number flow, where the inertia is completely neglected.

Based on the previous works by Stone *et al.* (1986) and Stone & Leal (1989), Qian & Law (1997) proposed a schematic of the end-pinching mechanism. The rounded end gives larger curvature than the midsection of the ligament, which leads to a higher internal pressure near the end than that in the cylindrical section. This pressure difference generates a local flow and drives the ligament end towards the midsection. Then, the bulbous ends are created due to the accumulation of mass, and this results in concavity near the ends. Consequently, a pressure minimum near the location with outward curvature creates a local flow moving towards the end. A neck is then formed to conserve the mass of the ligament, and the pressure in the neck region increases due to the large curvature. This pressure induces an additional flow towards the midsection, which further decreases the radius of the neck region. Finally, this unstable necking process leads to the pinch-off of the bulbous end. Ha & Leal (2001) extended the work by Stone *et al.* (1986) to study the elongation of a fluid drop at much higher shear rates. They found that the critical elongation ratio for the ligament breakup depends strongly on the shear rate.

Recently, using a coupled level set and volume-of-fluid method and by neglecting the dynamics effect of air, Tong & Wang (2007) simulated the time-dependent relaxation and pinch-off of a moderately elongated liquid droplet. The effect of the end shape on the breakup was investigated, and they found that the end shape plays a key role in the relaxation process. The underlying mechanism of the end-pinching was also examined, and they reported that the schematic of the end-pinching mechanism by Qian & Law (1997) was 'flawed', and a corrected explanation of the end-pinching

was proposed. In Tong and Wang's schematic, the maximum pressure appears a little bit upstream from the neck region where the radius is at a minimum as compared to Qian and Law's explanation, in which the maximum pressure resides right at the neck region. This is because the lateral curvature of the neck region creates a slightly concave surface, based on their numerical results, and thus decreases the surface tension forces. The local flow, which starts from the centre of the neck region, moves towards the centre of the midsection. They pointed out that the competition between the extending flow and the primary recoiling flow determines the breakup or reopening of the neck. It should be noted that a major difference between the above two proposed mechanisms lies in the surrounding fluids. Namely, in Tong and Wang's study, the surrounding fluid, i.e. air, is neglected. Thus the viscosity and density ratio are both infinity; while Qian and Law's explanation is based on the investigations by Stone *et al.* (1986) and Stone & Leal (1989), in which the viscosity ratios are between 11.3 and 0.01, and the densities of the both fluids are almost matched in order to minimize the buoyancy effect.

The goal of this paper is to perform a detailed investigation of the underlying physics of the relaxation and breakup of an elongated droplet, especially for the end-pinching mechanism, using a three-dimensional direct numerical method. We simulate cases with a large range of viscosity ratio and/or large density ratio. In particular, compared to the work by Stone & Leal (1989), the present cases are more general in that both the inertial and viscous forces are considered, and in contrast to the simulations by Tong & Wang (2007), the suspending flow effects are included. By employing mesh adaptations locally, the present study can capture the necking process to as little as 1 % of the initial droplet radius. In addition, the full Navier–Stokes calculations shall be used to depict the whole fluid field in space, which provides us a better understanding of the underlying physics.

In recent years, a number of numerical methods were developed and have been successfully used to simulate incompressible and immiscible two-phase flow. Volume of fluid (Chen *et al.* 1999; Scardovelli & Zaleski 1999), front tracking (Unverdi & Tryggvason 1992; Mortazavi & Tryggvason 2000; Hua & Lou 2007), level set (Sussman, Smereka & Osher 1994; Sussman & Smereka 1997), level set coupled with adaptive unstructured volume remeshing (Zheng *et al.* 2005) and immersed-boundary (Peskin 1977; Li & Lai 2001) methods are a few examples. In most of the above methods, the Navier–Stokes equations are solved on a background mesh, and the jumps in the fluids' properties and the normal stresses (normally, surface tension forces) across the interface are usually smoothed in a finite thickness interface region. The boundary integral method (Stone & Leal 1989; Zhou & Pozrikidis 1993; Cristini, Blawzdziewicz & Loewenberg 2001) is used to accurately capture the interface dynamics for Stokes flows, where the interface is of zero thickness.

In this paper, three-dimensional direct numerical simulations of the relaxation and breakup of an elongated droplet are performed by solving the full Navier–Stokes equations for the two-phase flow system using a finite volume method, coupled with a moving mesh interface tracking (MMIT) scheme to locate the interface (Quan & Schmidt 2007). The viscosity ratio is in the range of 0.1–100 and density ratio in the range of 1–100. The Ohnesorge number, which relates the viscous and surface tension forces, is in the range of 3.73×10^{-4} to 1.18, which implies that the Reynolds numbers based on the surface tension forces are significantly greater than unity. The effects of the viscosity ratio, density ratio and length ratio on the overall relaxation process are investigated. The effects on the detailed physics near the breakup point are also studied. The previously proposed end-pinching mechanisms (Stone *et al.* 1986; Stone

& Leal 1989; Qian & Law 1997; Tong & Wang 2007) are further examined, and more general end-pinching explanations are proposed based on the detailed analysis of the fluid field and the shape of the neck region. By examining the fluid velocity field, it is found that the different vortex ring patterns are the key reason for the disparate neck shapes. In the MMIT method, the interface is represented as a surface triangle mesh, and is therefore zero thickness. So the jumps in the fluid properties and the normal stresses are implemented directly, without any smoothing. Localized mesh adaptations on the interface and the interior tetrahedral cells are employed to maintain good mesh quality, to capture the curvature variation, to deal with large deformation and also to achieve computational efficiency. Topological transition in the two-phase flow simulations, such as breakup, is a challenge for the MMIT. To address this challenge, a mesh separation scheme is applied.

2. Problem formulation

The transient motion of the relaxation and breakup of a moderately elongated droplet in another viscous fluid is governed by the Navier–Stokes equations. The two fluids are assumed incompressible and immiscible, and there is no phase change in the process. The two fluids are initially at rest.

Normally, the Navier–Stokes equations are presented in a form which is derived for a fixed control volume, where the shape, the position and the volume do not change with time. However, in a two-phase flow scenario, such as ligament relaxation and pinch-off, the interface moves with the fluid, and the interface is an ideal surface for the control volume having an interfacial surface. So it is more convenient for us to use the integral form of the Navier–Stokes equations in a moving and deforming control volume for the two incompressible and immiscible fluids as

$$\frac{\mathrm{d}}{\mathrm{d}t}\iiint_{CV}\mathrm{d}v=\iint_{CS}\boldsymbol{v}\cdot\boldsymbol{n}\,\mathrm{d}s, \tag{2.1}$$

$$\frac{\mathrm{d}}{\mathrm{d}t}\iiint_{CV}\rho\,\mathrm{d}v+\iint_{CS}\rho(\boldsymbol{u}-\boldsymbol{v})\cdot\boldsymbol{n}\,\mathrm{d}s=0, \tag{2.2}$$

$$\frac{\mathrm{d}}{\mathrm{d}t}\iiint_{CV}\rho\boldsymbol{u}\,\mathrm{d}v+\iint_{CS}\rho\boldsymbol{u}(\boldsymbol{u}-\boldsymbol{v})\cdot\boldsymbol{n}\,\mathrm{d}s=\iiint_{CV}\rho\boldsymbol{f}\,\mathrm{d}v-\iint_{CS}p\boldsymbol{n}\,\mathrm{d}s+\iint_{CS}\mu(\nabla\boldsymbol{u}+\nabla\boldsymbol{u}^{T})\cdot\boldsymbol{n}\,\mathrm{d}s, \tag{2.3}$$

where CV and CS denote a control volume and the surfaces of the control volume, $\boldsymbol{u}$ is the fluid velocity, $\boldsymbol{v}$ stands for the surface velocity of the moving and deforming control volume, $\boldsymbol{n}$ is the unit normal vector of the face, $\boldsymbol{f}$ denotes the body force per unit mass and the superscript T stands for the transpose. It should be noted that (2.1) is a consistency requirement for the volume of a moving and deforming control volume that can be derived from Leibnitz's theorem. It also should be noted that the convection terms in (2.2) and (2.3) are identically zero on the interface if the interface moves with the fluid velocity, i.e. $\boldsymbol{u}=\boldsymbol{v}$. Therefore, the jump in the fluid's density across the interface presents no numerical difficulties for the MMIT method.

The interface is an internal boundary in the two-phase flow, and the fluid properties are normally discontinuous across this boundary. Therefore, there must be some boundary conditions across the interface for solving the above Navier–Stokes equations. From conservation of mass (2.2), if an infinitesimally thin control volume

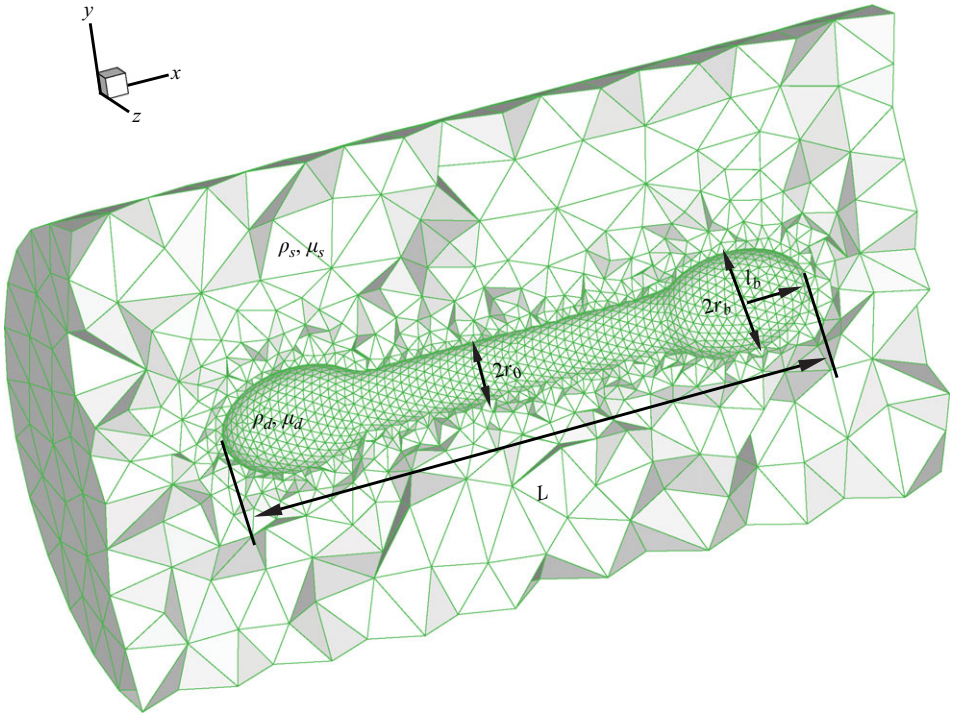

FIGURE 1. Schematic of the physical and computational domain of an elongated droplet in another fluid. The domain mesh is also shown. The ligament is in the centre with the finer mesh.

is applied to the interface, we have

$$u_{1n} = u_{2n} = v_n, \tag{2.4}$$

where the subscript n stands for the normal component, and the subscripts 1 and 2 denote phase 1 and phase 2. This indicates that the normal velocities of the two fluids near the interface are continuous, and should equal the normal velocity of the moving interface in order to satisfy the conservation of mass for each phase. Because the two fluids are viscous, the tangential velocities of the two fluids near the interface should be continuous. From the conservation of linear momentum (2.3), and considering the surface tension forces on the interface, the jump condition of the normal stresses is

$$[\![p]\!] = -\sigma\left(\frac{1}{R_1} + \frac{1}{R_2}\right) + [\![\,2\mu\,(\nabla \boldsymbol{u}\cdot\boldsymbol{n})\cdot\boldsymbol{n}]\!], \tag{2.5}$$

where $[\![\cdot]\!]$ denotes the difference across the interface, σ stands for the surface tension coefficient and is assumed constant to avoid Marangoni effects, R_1 and R_2 are the principle radii of the surface. It should be noted that the jump in the normal stresses includes not only the surface tension forces but also the difference in the normal viscous stresses. The continuity condition of the shear stresses is expressed as

$$[\![\mu((\nabla \boldsymbol{u} + \nabla \boldsymbol{u}^T)\cdot\boldsymbol{n})\cdot\boldsymbol{\tau}]\!] = 0, \tag{2.6}$$

where $\boldsymbol{\tau}$ denotes the unit tangential vector.

The physical problem and the computational domain are sketched in figure 1, and the mesh is also shown. The outer domain is a cylinder with a coarse mesh and filled with a viscous liquid. A no-slip boundary condition is imposed on the cylinder walls

including the two end surfaces. An initially elongated droplet with a radius of r_0 of the cylindrical section is located at the centre of the computational domain and discretized with a fine mesh. The ligament has two bulbous ends, and the shapes of the two ends are ellipsoidal (see Stone & Leal 1989; Tong & Wang 2007). The longest and the shortest axes for the ellipsoid are $2.6r_0$ and $1.7r_0$, as defined in figure 1, for the simulation reported here. The connection between the central cylinder and the end ellipsoids is blended smoothly to avoid any irregularity. The total length of the ligament is L. The suspending fluid has a viscosity of μ_s and a density of ρ_s, and the viscosity and the density for the elongated droplet are μ_d and ρ_d, respectively. The liquid properties for the droplet are kept constant for all the simulations. The effect of the density and the viscosity ratios on the relaxation and breakup process is studied by varying the fluid properties of the suspending phase. Initially, the two fluids are at rest. Gravity is neglected in all the simulations; thus buoyancy forces are absent for any density difference. The density ratio is defined as $\eta = \rho_d/\rho_s$, the viscosity ratio as $\lambda = \mu_d/\mu_s$ and the length ratio as $\kappa = L/r_0$. Then, the characteristic time based on the radius of the cylindrical section (r_0) is $t_c = r_0\mu_d/\sigma$. The Ohnesorge number based on the droplet properties is defined as $Oh_d = \mu_d/\sqrt{\rho_d\sigma r_0}$, and $Oh_s = \mu_s/\sqrt{\rho_s\sigma r_0}$ for the Ohnesorge number based on the suspending fluid properties. Here, an effective Reynolds number is defined based on u_c ($u_c = \sqrt{\sigma/\rho_d r_0}$) as $Re = \sqrt{\rho_d\sigma r_0}/\mu_d$, which is the inverse of Oh_d. The characteristic kinetic energy per unit mass is $e_c = \sigma/2\rho_d r_0$.

3. Numerical method and mesh adaptation

The unsteady motion of the ligament relaxation and breakup in another fluid is simulated by a staggered finite volume MMIT method to capture the deforming and moving interface. The governing equations (2.1), (2.2) and (2.3) are discretized by a finite volume method in a strongly conserved form as following (for details, see Dai *et al.* 2002; Zhang, Schmidt & Perot 2002; Perot & Nallapati 2003; Dai & Schmidt 2005; Quan & Schmidt 2007):

$$\frac{V_c^{n+1} - V_c^n}{\Delta t} = \sum_{cell\ faces} U_f^{mesh}, \tag{3.1}$$

$$\frac{\rho_c^{n+1}V_c^{n+1} - \rho_c^n V_c^n}{\Delta t} + \sum_{cell\ faces} \rho_f\left(U_f - U_f^{mesh}\right) = 0, \tag{3.2}$$

$$\frac{\rho_c^{n+1}\boldsymbol{u}_c^{n+1}V_c^{n+1} - \rho_c^n\boldsymbol{u}_c^n V_c^n}{\Delta t} + \sum_{cell\ faces} \rho_f\boldsymbol{u}_f\left(U_f - U_f^{mesh}\right) = -V_c^{n+1}\nabla\left(p - \rho_c\boldsymbol{f}\cdot\boldsymbol{r}_c^{CG}\right)^{n+1}$$
$$+ \sum_{cell\ faces} 0.5\left[(\mu\nabla\boldsymbol{u}_f\cdot\boldsymbol{n}_f A_f)^n + (\mu\nabla\boldsymbol{u}_f\cdot\boldsymbol{n}_f A_f)^{n+1}\right] - \left(V_c\left(\boldsymbol{f}\cdot\boldsymbol{r}_c^{CG}\right)\nabla\rho_c\right)^{n+1} \tag{3.3}$$

and the convection term is computed by central differencing in time and a predictor corrector scheme:

$$\sum_{cell\ faces} \rho_f\boldsymbol{u}_f\left(U_f - U_f^{mesh}\right) = \sum_{cell\ faces} 0.5\rho_f\left[\boldsymbol{u}_f^n\left(U_f - U_f^{mesh}\right)^n + \boldsymbol{u}_f^{n+1}\left(U_f - U_f^{mesh}\right)^{n+1}\right]. \tag{3.4}$$

The viscous and convection terms are calculated in a similar scheme, i.e. a centred difference in time with a predictor–corrector scheme, and are second-order accurate (Zhang *et al.* 2002). It should be noted that in the simulations, the gravitational force

$\boldsymbol{f}$ is neglected. The moving mesh face flux U_f^{mesh} is computed from the displacement of the face nodes as (Perot & Nallapati 2003)

$$U_f^{mesh} = \frac{\boldsymbol{x}_f^{n+1} - \boldsymbol{x}_f^n}{\Delta t} \cdot \left[\frac{1}{2}\left(\boldsymbol{n}_f^{n+1} A_f^{n+1} + \boldsymbol{n}_f^n A_f^n\right) - \frac{\Delta t^2}{12} \sum_{face\ edges} (\boldsymbol{v}_{n1} \times \boldsymbol{v}_{n2}) \right]. \tag{3.5}$$

Here, U_f is the face flux, V_c denotes the cell volume, $\boldsymbol{r}_c^{CG}$ stands for the position vector of the cell centroid, A_f is the face area, the superscript n stands for the time step, $\boldsymbol{x}$ is the node position, $\boldsymbol{v}_n$ stands for the node velocity and the subscripts c and f denote the cell and face respectively.

The computational domain for both the ligament and the suspending phases is discretized by tetrahedral meshes with much finer meshes in the droplet phase, as shown in figure 1. The interface is represented by triangle meshes which connect the meshes of the ligament phase and the suspending fluid phase to a single mesh. The Navier–Stokes equations are solved in a discrete stream function formulation; thus the mass conservation is satisfied automatically (Perot & Nallapati 2003). Three-dimensional stream function vectors ($\boldsymbol{u} = \nabla \times \boldsymbol{s}$ with $\boldsymbol{u}$ representing velocity and $\boldsymbol{s}$ a stream function vector) are defined at the edge centres. The face fluxes and the cell-centre velocities can be constructed from the stream function vectors by using Stokes' theorem and Gauss' divergence theorem. An exact fractional step method (Chang, Giraldo & Perot 2002) is employed to avoid solving a Poisson equation for pressure. A three-step second-order low-storage Runge–Kutta scheme is used for time integration (Perot & Nallapati 2003). The time step is limited by Courant–Friedrichs–Lewy (CFL) number ($\Delta t \leqslant \frac{CFL \cdot \Delta x}{U}$), surface tension ($\Delta t \leqslant C\sqrt{\rho \Delta x^3 / 2\pi\sigma}$) and mesh Péclet numbers ($2 \cdot CFL \leqslant Pe \leqslant 2/CFL$), where U is a characteristic velocity, C is a constant and usually is chosen the same as the CFL number (Quan & Schmidt 2007).

The mesh vertices on the interface move in a Lagrangian fashion with the fluid velocity to conserve the mass of each phase and to avoid any mixing, while the interior vertices are free to move in order to maintain mesh quality. Mesh motion alone is not sufficient to provide adequate mesh quality; as the mesh moves, changes in mesh connectivity are required. In order to have near-optimal connectivity, to capture the large variation of the curvature on the interface, and to achieve computing efficiency as well as accuracy, mesh adaptation schemes on tetrahedral meshes, such as, 3-2 and 2-3 flips, 4-4 swaps, edge bisections, edge contractions and an optimization-based smoothing (Dai & Schmidt 2005; Quan & Schmidt 2007) are employed. A mesh separation scheme is applied to deal with the breakup. The capability of the mesh adaptations and the mesh separation has been tested by numerous cases of two-phase flow (Quan & Schmidt 2006, 2007) and single phase flow (Dai & Schmidt 2005).

As mentioned in the last section, the jump in the fluid's density across the interface is automatically taken care of in the MMIT method. However, the viscosity on the interface is not defined. The geometric harmonic mean (Quan & Schmidt 2007) is used to calculate the viscous shear stresses on the interface, and is second-order accurate. Previously, Liu, Fedkiw & Kang (2000) derived a similar scheme, but in a different context. The surface tension force is calculated using a least squares parabola fitting in a local coordinate system, and is implemented as a pressure boundary condition. The jump in normal viscous stresses is implemented directly by using Taylor series expansion to the first order for a multivariable function.

The numerical method is capable of accurately simulating the two-phase flows with high density and viscosity ratios and has been validated against a number of experimental observations and theoretical predictions (Quan & Schmidt 2006, 2007).

In particular, a zero-gravity three-dimensional droplet oscillation in a gaseous flow with Oh_d of 0.013 was computed and compared with the analytical solution by Lamb (1945). The relative errors of the oscillation period and the decay factor are 0.9 % and −0.4 %, respectively. The numerical simulation is capable of accurately capturing the oscillation for 8 periods. This droplet oscillation is fundamentally similar to the ligaments considered in this paper with the driving force being the surface tension and both fluids being viscous. The significant difference between the droplet studies and the current work is the initial shape. Another test case is a droplet under shear with a capillary number of 0.05 ($Ca = \mu_s R_0 \dot{\gamma}/\sigma$, where R_0 is the radius of the spherical droplet and $\dot{\gamma}$ denotes the shear rate). The computed deformation factor of 0.076, agrees well with the experimental result, 0.07, by Taylor (1934). A mesh dependence study has been performed in Quan & Schmidt (2006), and it was found that the results for the coarse mesh agreed very well with the ones for the finer mesh.

4. Results and discussion

In this section, the results of the relaxation and breakup of a moderately elongated droplet in another viscous fluid are reported and discussed. The effects of the viscosity ratio, the density ratio and the length ratio on the relaxation and breakup process are investigated. A detailed examination of the end-pinching mechanism is also presented. A fixed length ratio of 20, as shown in figure 1, is used to investigate the viscosity ratio effect and the density ratio influence.

4.1. *Mesh adaptation and mesh separation*

As the interface moves with the fluids, in order to capture the interesting physics which occur near the interface, it is important to ensure that the mesh adaptation scheme is capable of maintaining good mesh quality. The relaxation of an elongated droplet with $\eta = 10$, $\lambda = 0.1$, $\kappa = 20$, and $Oh_d = 0.037$, $Re = 27.03$, $Oh_s = 1.18$ is employed to show the capability.

Figure 2 shows the surface mesh and the interior mesh of the ligament relaxation near the time of the breakup. Here, the time of the breakup is the moment that the mesh separation scheme is applied. In this case, it occurs when the smallest radius of the neck region is around 2.4 % of the radius of the cylinder section of the original elongated droplet. Compared to the radius of the end droplet shown in the figure 2, the neck region radius is only around 1 %. Figure 2(*a*) displays the interface mesh for the ligament. The cells in the neck region are hardly perceivable due to the resolution required to capture the interface curvature. Details of the mesh in the neck region are clearly displayed in the enlarged view in figure 2(*c*). It can be seen that the surface mesh quality is good, and the transition from the finest mesh in the neck region to the mesh of the droplet is smooth. The interior mesh at the breakup moment for both the droplet phase and the suspending fluid are shown in figure 2(*b*). For clarity, the suspending fluid is shaded lighter, and the droplet shaded darker. It should be noted that, although different shade levels are used to display the two phases, the simulations use a single mesh for the whole domain. The mesh near the interface, where the most interesting physics occur, is so fine that it is difficult to see the individual cells, while the mesh far away from the interface is very coarse, and the largest cells are near the boundaries where the fluid is almost at rest.

A mesh separation scheme is needed for simulating pinching off into separate droplets. Mesh separation is implemented as: (i) convert the fluid properties of the droplet cells in the neck region to the properties of the suspending fluid; (ii) project

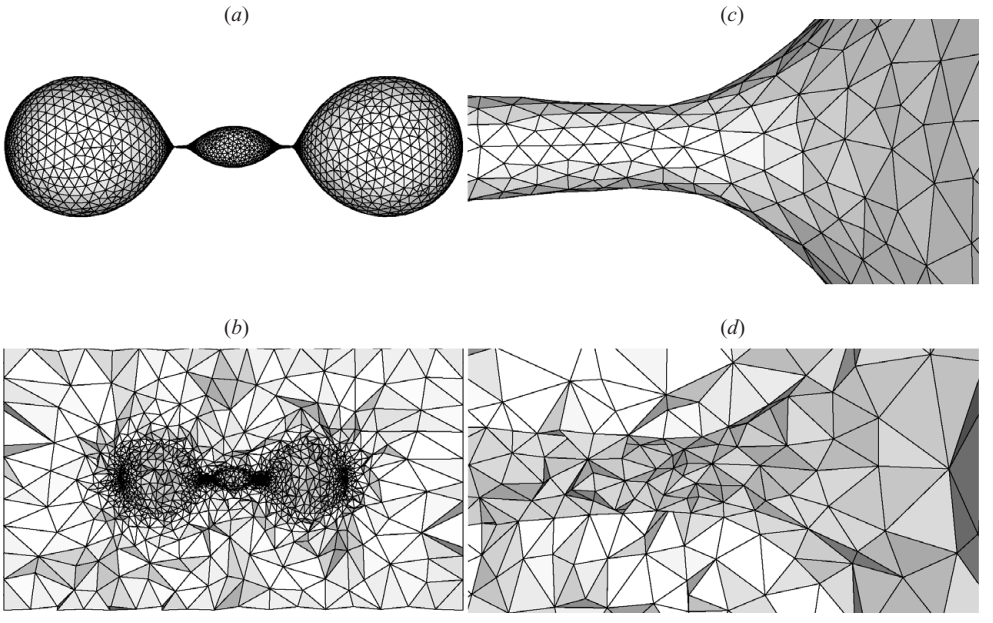

FIGURE 2. Mesh adaptation for the interfacial and the interior meshes before the pinch-off: $\eta = 10$, $\lambda = 0.1$, $\kappa = 20$, and $Oh_d = 0.037$, $Oh_s = 1.18$. (*a*) Mesh for the ligament just before pinch-off in the x–y plane; (*c*) enlarged view of the mesh in the neck region; (*b*) mesh for the whole domain just before pinch-off. The lighter shade stands for the suspending phase, and the mesh for the elongated droplet is shaded darker; (*d*) blow-up view of the interior mesh at the neck region. Here 50 % depth blanking from the front in the z direction (cells near the central plane) is applied in (*b*) and (*d*).

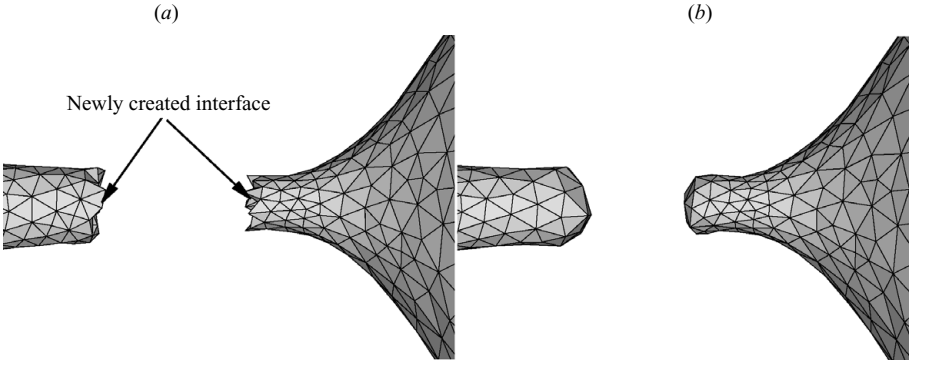

FIGURE 3. Mesh separation. (*a*) Interface meshes after the conversion. The two newly created interfaces are rough. (*b*) Interface meshes after the projection. The interface meshes are much smoother. Only the surface mesh of the droplet phase is displayed.

the new created interface face nodes to a local hemisphere to smooth the newly created rough interface. The details of the scheme can be found in Quan & Schmidt (2007) and Quan, Lou & Schmidt (2009). Figure 3(*a*) shows the mesh just after the conversion, and it can be seen that the newly created interfaces are too irregular to continue the computation because the calculated surface tension forces would have huge random errors. The smoothed interface is displayed in figure 3(*b*): it is clear the interface is much smoother and the calculation can be continued. The portion of

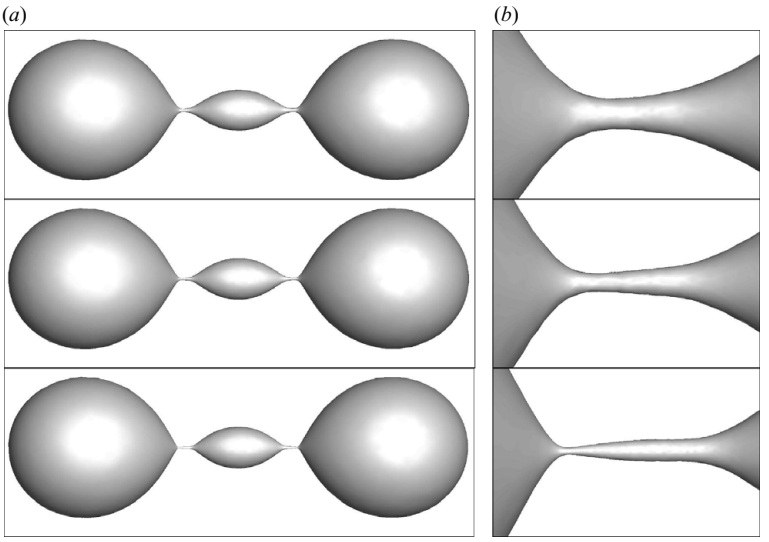

FIGURE 4. Comparison between the smallest neck radius of 5 %, 2.4 % and 1 % at $t = 507.2$, 509.8 and 511.8 from the top to the bottom, respectively. (*a*) The overall shape; (*b*) a detailed view of the neck region of (*a*).

the droplet in the neck region which is converted to the suspending fluid should be very tiny compared to the whole droplet to minimize the mass loss of the droplet and mass gain of the suspending fluid.

The cutoff neck radius was varied from 5 % to 1 % of the initial droplet radius in order to check for resolution sensitivity. Figure 4 shows the comparison of the three cases. It is noted that the differences of the overall shape are minimal; by allowing smaller neck radius, the pinch-off is slightly delayed. There are a few differences in the small-scale features of the neck region in the shape and size. With the change in cutoff neck radius by more than a factor of 2, the mass differences of the droplets (the two primary drops and the middle satellite, respectively) are as small as 0.5 % and the differences of the distances between created droplets are less than 0.8 %. Qualitatively, the different cutoff radius very slightly retards the development of some of the very small-scale features just after pinching.

4.2. *Viscosity ratio effect*

The viscosity ratio is one of the governing non-dimensional parameters for the droplet relaxation and breakup, so it is of interest to understand the effect of the viscosity ratio on the process. Figure 5 shows the sequences of the relaxation and breakup for the ligament with bulbous ends for different viscosity ratios, i.e. $\lambda = 0.1$, 10 and 100. The density ratio is 10, and the Ohnesorge number based on the droplet properties is 0.037. The droplet is shaded by its extension in the radial direction, and the times are non-dimensionalized by the characteristic time $t_c = r_0\mu_d/\sigma$. The separation scheme is applied to the simulations here and thereafter when the neck region is very narrow (typically less than 5 % of r_0).

To ensure that the outer walls do not significantly affect the process, a larger domain for the case with density ratio of 10 and viscosity ratio of 100 was simulated and compared to the one with the domain as shown in figure 1, where the smallest distances from the outer walls to the ligament in axial and radial directions for the larger domain are two times of the distances for the smaller domain. It was found

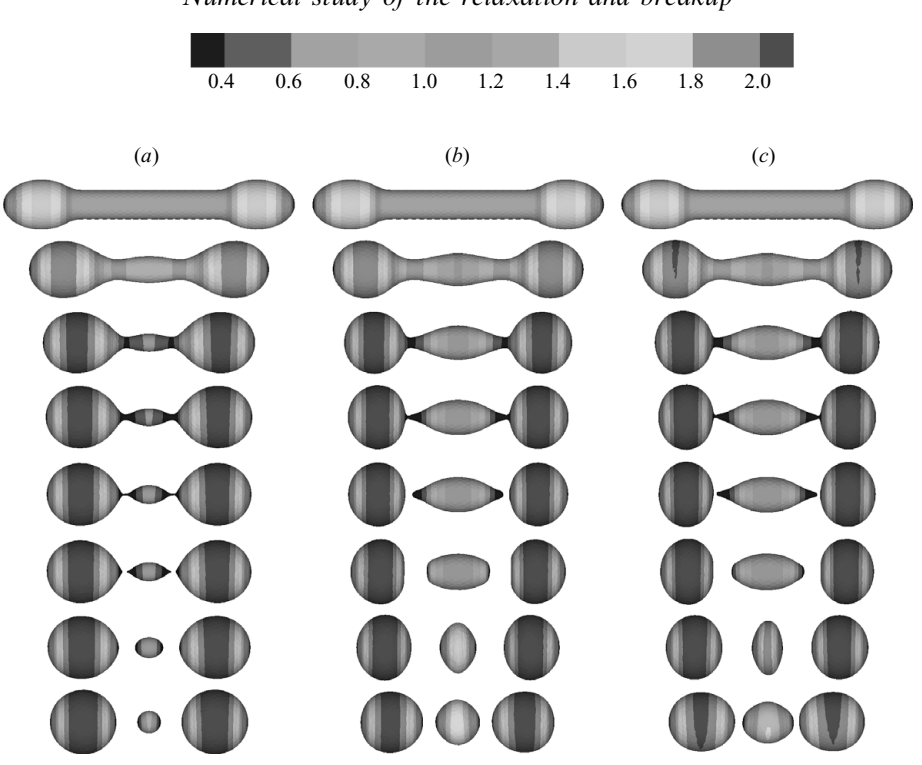

FIGURE 5. The effect of the viscosity ratio on the relaxation and breakup of an elongated droplet immersed in another viscous fluid. The droplets are shaded by the non-dimensional radius (r/r_0) in the radial direction, and the contour legend is on the top of the figure: $\eta = 10$, $\kappa = 20$ and $Oh_d = 3.7 \times 10^{-2}$. (*a*) $\lambda = 0.1$; $Oh_s = 1.18$; $t = 0.0$, 251.3, 435.3, 489.6, 509.8, 511.2, 532.9, 613.7. (*b*) $\lambda = 10$; $Oh_s = 1.18 \times 10^{-2}$; $t = 0.0$, 108.0, 144.1, 158.5, 159.8, 169.2, 199.2, 242.4. (*c*) $\lambda = 100$; $Oh_s = 1.18 \times 10^{-3}$; $t = 0.0$, 108.0, 144.0, 157.0, 158.5, 165.6, 201.7, 244.9.

that the differences are minimal, so for all the simulations presented in this paper, the smaller domain is used.

4.2.1. *Shape evolution*

Figure 5(*a*) shows an evolution of the transient behaviour of elongated droplet relaxation and pinch-off with a viscosity ratio of 0.1. The Ohnesorge number based on the suspending fluid's properties is 1.18. First, due to the large surface tension forces at the two ends, the two bulbous ends move towards the centre, and at the same time, necking occurs near the two ends in the middle section, which can be seen at time of 251.3. Then due to the large surface tension force at the neck region, the neck becomes increasingly narrower until it breaks up at a time slightly larger than 509.8. After the breakup of the two bulbous ends, the middle section has a shape with two nearly pointed ends. The two pointed ends move towards the centre due to huge surface tension forces, and finally a spherical satellite droplet is obtained due to the great viscous damping from both phases. Figures 5(*b*) and 5(*c*) show a series of relaxation and pinch-off history for the cases with viscosity ratio of 10 and 100 respectively. The relaxation and breakup processes for these two cases are similar. Necking regions near the two bulbous ends are created, and then the curvature of the neck regions becomes increasingly large, and finally two large droplets pinch off. A middle section with two somewhat pointed ends is formed, and these two ends

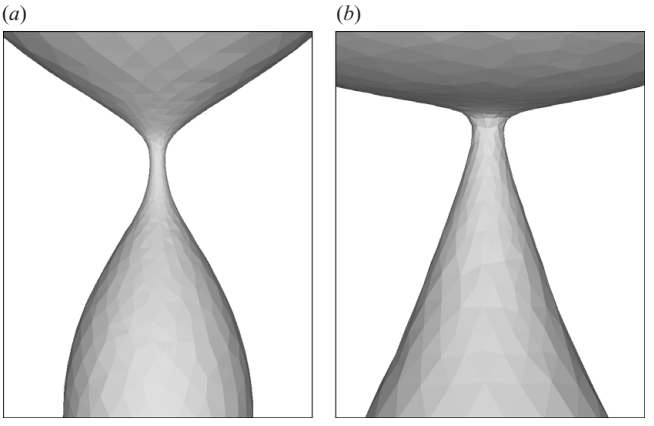

FIGURE 6. Blow-up view of the neck shape showing the difference in the symmetry. (*a*) The case in figure 5(*a*) with $\lambda = 0.1$; (*b*) the case in figure 5(*c*) with $\lambda = 100$.

contract towards the centre. Meanwhile, the two newly formed droplets are dimpled at the inner side, especially for the case in figure 5(*b*) at $t = 169.2$. Then, the middle section experiences damped oscillation and so do the two end droplets.

Comparing figures 5(*a*), 5(*b*) and 5(*c*), we can observe some interesting differences. The neck shape just before the breakup for the viscosity ratio of 0.1 is much different from the shape of the other two cases where the viscosity ratio is greater than one. A detailed view of the neck shapes is shown in figure 6 with the droplet shaded grey. Figure 6(*a*) shows the neck shape for $\lambda = 0.1$, and figure 6(*b*) shows it for $\lambda = 100$. It can be seen clearly that the pinch-off region for $\lambda = 0.1$ is approximately a cylinder of revolution and is almost symmetric around a plane transverse to the ligament axis. However, the shape for the $\lambda = 100$ case is conical, and there is no such symmetry about the plane perpendicular to the relaxation direction. Burton, Waldrep & Taborek (2005) performed experiments on the water–air systems using high-speed microscopy and reported the similar distinction in the shape of the neck region between an air bubble in water and a water droplet in air. Although the governing equations for the two systems are similar, the roles of the high and low viscosity (or density) fluids are reversed, and this leads to differences in the flow pattern (a detailed discussion is followed in § 4.2.3) and thus resulting different shapes of the breakup regions. This 'quadratic' shape was also observed by Doshi *et al.* (2003). The conical shape of the neck region for the more viscous droplet pinch-off in a less viscous fluid were also reported previously (e.g. Eggers 1997; Lister & Stone 1998; Zhang & Lister 1999; Burton *et al.* 2005).

Second, after the two end droplets pinch off, the relaxation processes of the middle section for the different viscosity ratio cases are also distinctly different. For the low-viscosity ratio case with $\lambda = 0.1$, due to the higher viscosity forces from the suspending flow, the relaxation process is retarded, and the pointed middle section becomes a spherical droplet very quickly without further oscillation. For the higher viscosity ratio cases ($\lambda = 10$ and 100), the relaxation and the necking are much faster as viscous damping from the suspending flow is weaker. The two nearly pointed ends of the middle section move towards the centre quickly due to the large surface tension forces. Because the damping from the suspending flow is smaller, the velocity at the two ends is large, and then an oblate spheroid is formed. The middle section will experience oscillation until the energy is damped out by the viscous forces. It should be noted

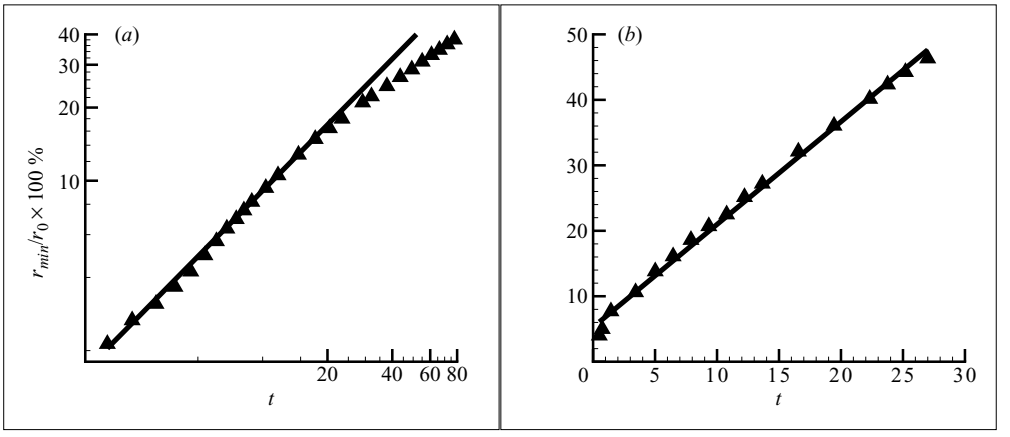

FIGURE 7. Evolution of the minimum neck radius. t is the time before the pinch-off and is non-dimensionalized by t_c. (*a*) Log–log plot for $\lambda = 0.1$ (figure 5*a*). The line has a slope of 0.89. (*b*) $\lambda = 100$ (figure 5*c*).

that the volumes of the satellite droplets of the two larger viscosity ratio cases are greater than the one with viscosity ratio of 0.1. There are also some differences in the primary droplets. The primary droplets are dimpled in the inner side for the two high viscosity ratios (see figure 5*b* at $t = 169.2$ and figure 5*c* at $t = 165.6$), while there is no such dimpled shape for the small viscosity ratio.

4.2.2. *Neck radius*

The pinch-off process, especially the evolution of the minimum neck radius has been a subject of interest (e.g. Papageorgiou 1995; Eggers 1997; Cristini, Blawzdziewicz & Loewenberg 1998; Cohen & Nagel 2001; Chen, Notz & Basaran 2002; Burton *et al.* 2005; Keim *et al.* 2006; Thoroddsen, Etoh & Takehara 2007; Burton & Taborek 2008; Quan & Hua 2008). To quantify the necking process, the time evolution of the minimum neck radius ($r^* = r_{min}/r_0 \times 100\,\%$) for two cases is shown in figure 7, where time is the time left to pinch off and non-dimensionalized by t_c. For the $\lambda = 0.1$ case, the minimum neck radius decreases in a power law for r^* less than 20 %, as a straight line is fitted for the numerical solutions in a log–log plot. The exponent is 0.89. The power law was reported experimentally by Burton *et al.* (2005) and by Thoroddsen *et al.* (2007) with more details for a bubble pinch-off in a liquid of different viscosities. They found that the power law exponent varies from 0.5 to 1 for different external fluids. Thoroddsen *et al.* (2007) defined a Reynolds number based on the capillary viscous velocity as $Re_\mu = \rho D_i \sigma/\mu^2$, where D_i denotes the inner diameter of the needle. For $Oh_s = 1.18$ of the simulation, Re_μ is around 1.4. The nearest case by Thoroddsen *et al.* (2007) is $Re_u = 0.3$, which has an exponent of 0.94. It should be noted that in our cases, the only driving force is surface tension, while in the experiments by Burton *et al.* (2005) and by Thoroddsen *et al.* (2007), the buoyancy force acts as another driving force besides the surface tension force. This might lead to the difference in the exponents. For the case with $\lambda = 100$, the minimum neck radius decreases linearly in time, and the linear relationship was reported by Eggers (1997) for high-viscosity liquid jet breakup and by Cohen & Nagel (2001) for two-phase droplet pinch-off. This further validates the accuracy of the numerical method. Recently, for inviscid pinch-off, Burton & Taborek (2008) reported experimentally that the shape of the pinch-off region and the power law governing the neck radius evolution are distinctly

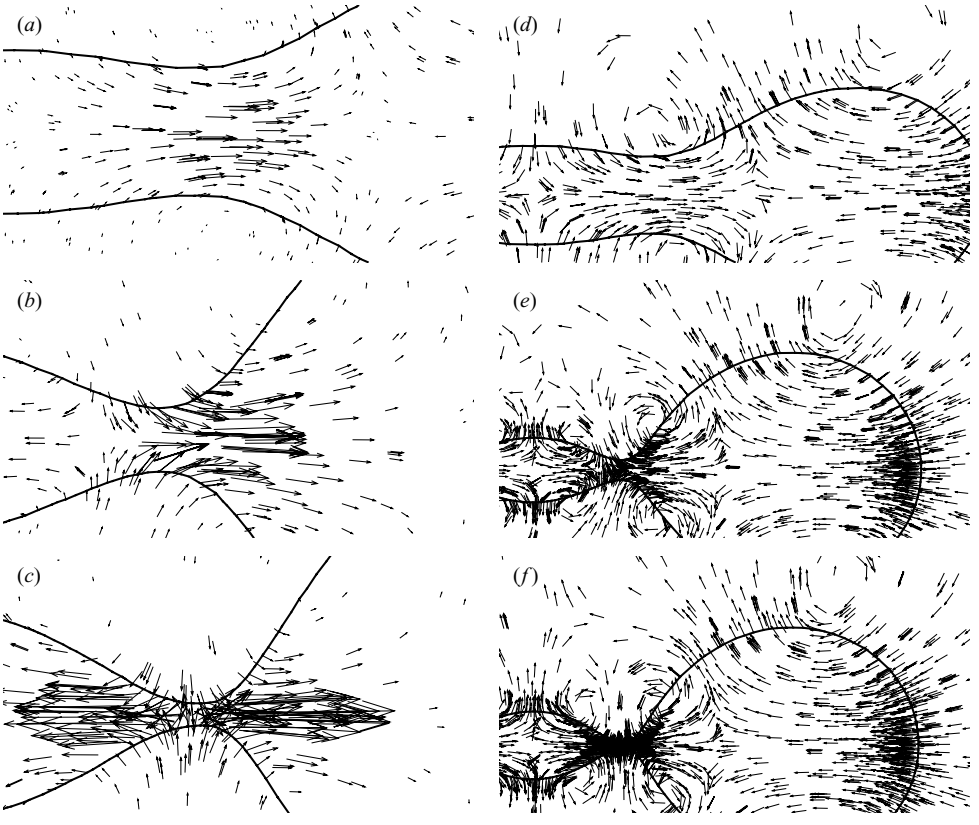

FIGURE 8. Detailed velocity fields of the necking process for the case of figure 5(*a*) ($\eta = 10$, $\lambda = 0.1$, $L/r_0 = 20$, $Oh_d = 0.037$ and $Oh_s = 1.18$) in the x–y plane. Figures (*d*)–(*f*) are the overall velocity field, and the vectors' lengths are unscaled to show the vortices. Figures (*a*)–(*c*) show enlarged views of the figures (*d*)–(*f*), and the velocity vectors are plotted with scaled lengths. (*a*) $t = 251.3$, (*b*) $t = 489.6$. and (*c*) $t = 506.2$.

different for low density ratio and high density ratio, and the transition happens at a density ratio around 0.25.

4.2.3. *Velocity field*

In order to explain the above differences and to understand the underlying physics, it is necessary to examine the fluid velocity field of the whole domain including both the suspending and droplet phases. Figures 8 and 9 show the velocity vectors and the neck shape for $\lambda = 0.1$ (the case in figure 5*a*) and $\lambda = 100$ (the case in figure 5*c*), respectively, at three representative times before breakup. The velocity vectors shown in figure 8(*a*–*c*) and figure 9(*a*–*c*) are scaled according to their magnitude. However, the lengths of the velocity vectors shown in figure 8(*d*–*f*) and figure 9(*d*–*f*) are unscaled in order to clearly show the vortices. It should be noted that our numerical simulations are three-dimensional calculations. The vortices shown in the figures are actually vortex rings about the x-axis because only a x–y plane cut of the whole domain is shown here (see figure 1 for the coordinate system).

From these developing velocity fields and the necking processes, a number of interesting observations can be made. There are vortex rings in the whole domain for the two cases, which can be seen clearly in figure 10. In the figure, the lines with

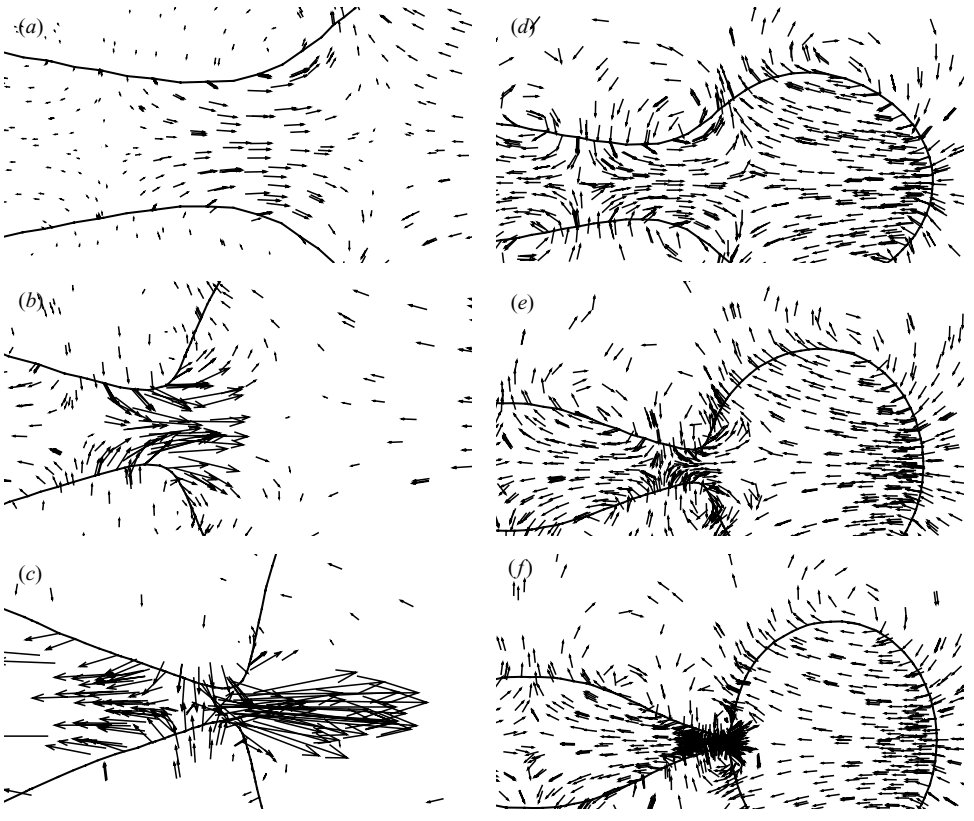

FIGURE 9. As in figure 8 but with $\lambda = 100$ (figure 5*c*), and $Oh_s = 1.18 \times 10^{-3}$. (*a*) $t = 108.0$, (*b*) $t = 144.0$ and (*c*) $t = 157.0$.

arrows are the streamlines in the x–y plane for the two cases just before breakup. The inner solid line is the ligament and the outer solid lines are the cylinder wall boundaries. To ensure that these circular streamlines actually represent the vortices in the domain, the vorticity is calculated for the case of figure 10(*a*) and is displayed in figure 11. Here, only the x–y plane cut is shown, and the level of the contour is based on the z component of the vorticity. The vorticity is non-dimensionalized by $\sigma/(r_0\mu_d)$. It is clear that the circular streamlines in the manuscript demonstrate the vortex rings in the fluid field. The maximum of the absolute value of the non-dimensional vorticity is around 1.5. However, in order to display all the vortex rings in the fluid field, the contour levels are chosen to range from -0.01 to 0.01. Therefore, it is more intuitive to observe the vortex rings using the streamlines.

In contrast, there are no vortex rings reported in Stone and Leal's numerical work (Stone & Leal 1989) using a boundary integral method. Vortex rings were observed in Tong and Wang's numerical simulation (Tong and Wang 2007) by solving the full Navier–Stokes equations. Their vortex centre is located inside the droplet, while it can be seen clearly that some vortex rings of our results are just outside of the interface and some are crossing the interface. This is due to the fact that in Tong and Wang's work, the dynamic effect of the suspending fluid (air) is neglected, while our numerical method directly solves the full Navier–Stokes equations for both fluids including the suspending and the drop phases.

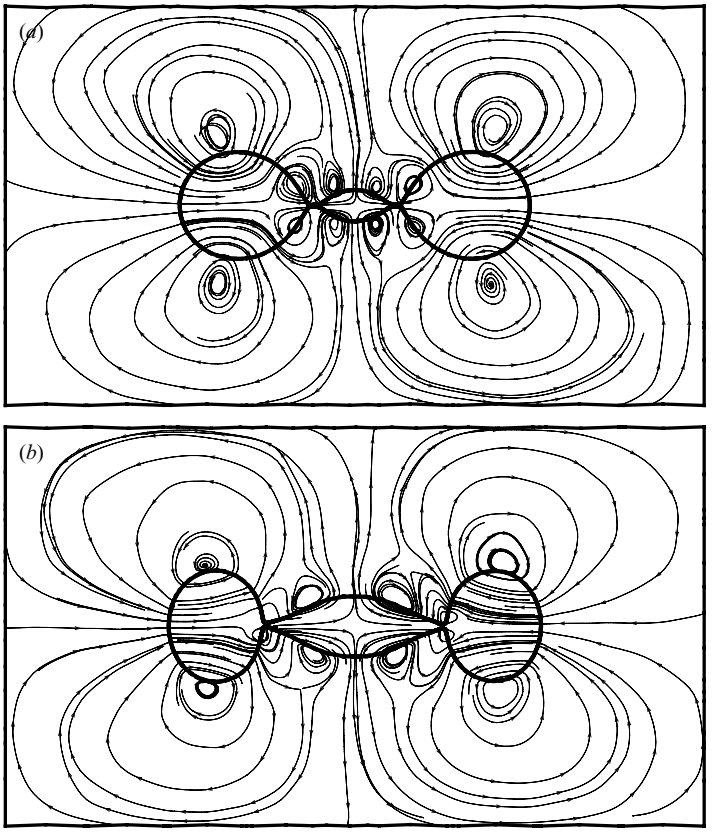

FIGURE 10. Vortex rings' pattern just before the breakup for the ligament with $\kappa = 20$. (a) Streamlines in the x–y plane for case of figure 5(a). (b) Streamlines in the x–y plane for case of figure 5(c). The outer solid lines are the boundary of the domain, and the inner solid lines are the shape of the droplet. Note that these streamlines are interpolated from three-dimensions and are approximate.

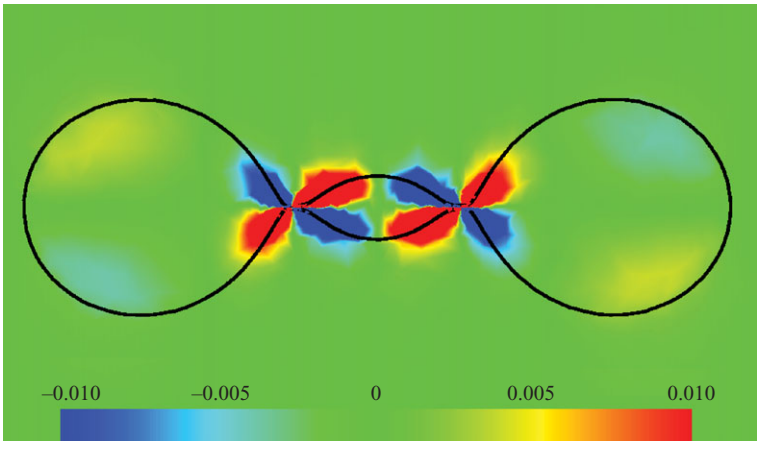

FIGURE 11. Vorticity contours in x–y plane of figure 10(a). The solid black lines denote the droplet shape.

Generation of vorticity at an interface has been an interesting subject for decades. Cresswell & Morton (1995) observed vortex rings in the experiments of a water droplet striking a water surface. They proposed that boundary condition of viscous stresses being continuous across the water–air interface accounts for the vorticity generated near the interface. Wu (1995) and Lundgren & Koumoutsakos (1999) pointed out that vorticity at the interface is generated as a result of the balance of shear stresses. The problem that we are solving contains two viscous immiscible fluids with continuity of the shear stresses across the interface. The large surface tension forces in the two ends drive the bulbous ends towards the centre, and the moving bulbous ends entrain the suspending flow from the surroundings. The high pressure near the neck region due to the large curvature drives liquid towards the ends, and moves the interface inwards. This motion of the interface near the neck also induces the suspending fluid to move towards the interface. Thus, vortices are created near the neck region and near the ends. It should be noted that in both cases, there are always an even number of vortex rings, and the vorticity alternates signs correspondingly (see figure 10). This indicates that the total circulation in the whole domain maintains zero as time progresses, which is anticipated for these axisymmetric cases.

It is also noted that the maximum velocity is near the neck region and the two ends. This is the result of large curvatures in these regions, and thus high pressure. However, there are some differences in both cases. The shape of the neck regions are different, as described in the previous discussion. The velocities, which are perpendicular to the direction of the relaxation, are at the portion of the neck region with the smallest curvature for the case with $\lambda = 0.1$, and the velocities near the neck region that move towards the end and towards the centre are almost symmetric. However, for the case with $\lambda = 100$ the velocities perpendicular to the relaxation direction are away from the position with the smallest curvature, and there is no symmetry of the velocities moving towards the centre and towards the end. These differences in the velocity field account for the distinct neck shape. There are also some discrepancies in the vortex rings for the two cases during the relaxation process. For the small viscosity ratio, there is only one vortex ring near the neck region of figure 8(*d*) where the necking is just beginning. As time progresses, there is one more vortex ring created on the left of the neck region, and the original large vortex ring becomes smaller (figure 8*e*). These two vortex rings are in opposite directions. Finally, the two vortex rings are similar in size just before the breakup (figure 8*f*). However, for the cases with larger viscosity ratio (figure 9), there are two vortex rings from the beginning of the necking, and the one on the left increases in size, while the one on the right decreases and is hardly perceptible at the time of the breakup.

4.2.4. *Kinetic energy*

We have shown previously that the viscosity ratio significantly affects the flow field and the shape of the neck region. We shall study the viscosity effects on the evolution of the ligament length and the history of the kinetic energy for both phases. The kinetic energy per unit mass is defined and numerically calculated as

$$KE = \frac{\iiint_{\Omega} \frac{1}{2}\rho u^2 \,\mathrm{d}v}{\iiint_{\Omega} \rho \,\mathrm{d}v} = \frac{\sum_{cells} \frac{1}{2}\rho_c u_c^2 V_c}{\sum_{cells} \rho_c V_c}, \tag{4.1}$$

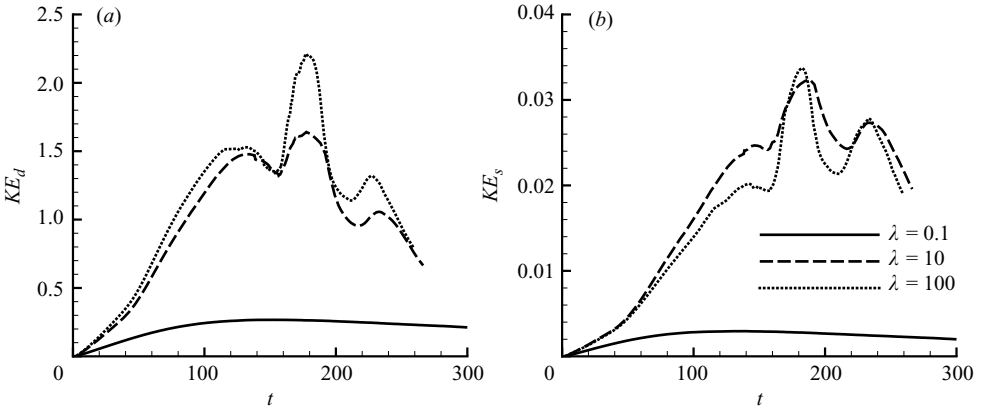

FIGURE 12. Viscosity ratio effect on the kinetic energy per unit mass for both phases. The three cases here are the same cases in figure 5. (*a*) Droplet phase, (*b*) suspending fluid.

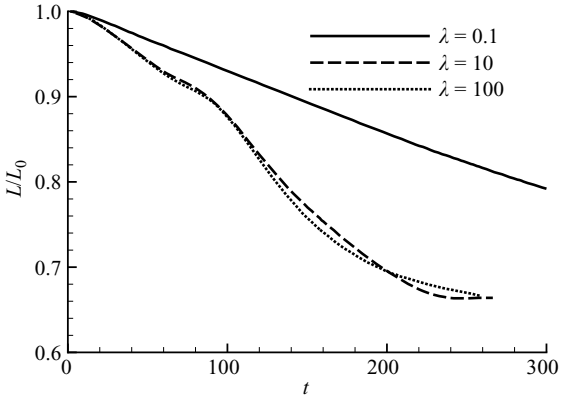

FIGURE 13. Viscosity effect on the evolution of the ligament length. The three cases here are the same cases in figure 5. The length is non-dimensionalized by its initial length.

where Ω denotes either the droplet phase or the suspending fluid, u_c is the cell velocity and V_c stands for the volume of a cell. Figure 12 shows the kinetic energy per unit mass for the droplet and the suspending flow. Here the kinetic energy is non-dimensionalized by $e_c = \sigma/2\rho_d r_0$, and time by $t_c = r_0\mu_d/\sigma$. The kinetic energy of the droplet for the large viscosity ratios ($\lambda = 10$ and 100) is much larger than that for the small viscosity ratio. This is because the more viscous ambient fluid more rapidly diffuses the momentum created by the surface tension forces, and thus less surface tension energy transforms to kinetic energy. The same trend is observed for the kinetic energy of the suspending flow. However, the kinetic energy for $\lambda = 100$ is not always larger than that for $\lambda = 10$. This indicates that, although the kinetic energy of the droplet for $\lambda = 100$ is always greater than the one for $\lambda = 10$, the energy transfer from the droplet to the suspending flow is larger for $\lambda = 100$, thus the suspending flow moves faster. It is noted that the kinetic energy for $\lambda = 0.1$ increases with time and reaches a maximum, and then decreases, while the kinetic energy for the two large viscosity ratios oscillates after it reaches a local maximum. The first peak represents the moment when the necking process is dominant, and the rest of oscillations denote the relaxation and shape oscillation of the middle section after breakup. Figure 13 displays the length variation versus time for the three cases. Figure 13 again suggests

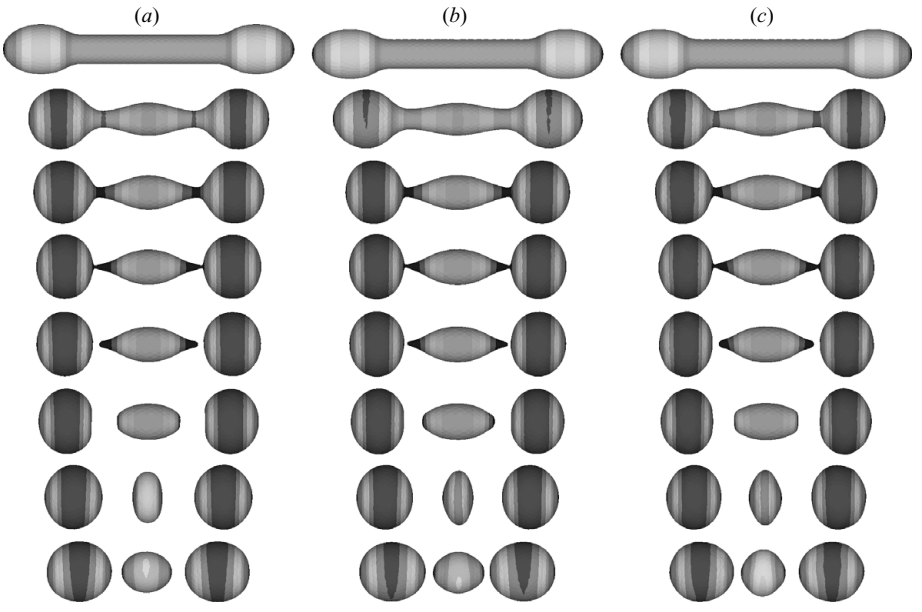

FIGURE 14. The effect of the density ratio on the relaxation and pinch-off process of the elongated droplet in a viscous fluid. The droplets are shaded the same as in figure 5: $\lambda = 100$, $\kappa = 20$ and $Oh_d = 3.7 \times 10^{-2}$. (*a*) $\eta = 1$; $Oh_s = 3.73 \times 10^{-4}$; $t = 0.0$, 144.0, 165.6, 180.1, 181.6, 194.5, 252.3, 297.0. (*b*) $\eta = 10$; $Oh_s = 1.18 \times 10^{-3}$; $t = 0.0$, 108.0, 144.0, 157.0, 158.5, 165.6, 201.7, 244.9 (*c*) $\eta = 100$; $Oh_s = 3.73 \times 10^{-3}$; $t = 0.0$, 115.4, 136.8, 147.7, 149.8, 158.5, 187.3, 223.3.

that the relaxation for the small viscosity ratio is slower than that for large viscosity ratios. The differences in the evolution of the ligament length and the kinetic energy further confirm that the pattern of the relaxation and pinch-off for the viscosity ratio greater than $O(1)$ is similar but distinctly different from the one for the viscosity ratio less than $O(1)$. These differences include the neck shape, the evolution of the minimum neck radius and also the pattern of the vortex rings.

4.3. *Density ratio effect*

It was shown in the last section that viscosity ratio significantly influences the relaxation and breakup of an elongated droplet. The effect of density ratio (one of the non-dimensional governing parameters) on the relaxation and pinch-off shall be investigated in this section. The length ratio ($k = L_0/r_0$) is 20, and the viscosity ratio is kept at 100. The surface tension coefficient is $\sigma = 7.2 \times 10^{-2}$ kg s^{-2} and kept constant. The density of the droplet is kept at 1.0×10^3 kg m^{-3}, while the density of the suspending fluids is varied to study the density ratio effect. Three density ratios (η) are simulated: namely, 1, 10 and 100.

Figure 14 shows the relaxation and the breakup of an initially elongated droplet with length ratio of 20 for three different density ratios. The droplets are shaded by the size of the radius, and the contour levels are the same as the one in figure 5. For the three different density ratios, the droplet experiences very similar process. The two ends move towards the centre due to the large surface tension forces at the ends. Then the droplet experiences necking and a conical shape of the neck region is created. Next, the neck pinches off, and two large droplets are generated. A nearly pointed middle section is created, and then undergoes relaxation and oscillation. The created satellite droplet in the middle is almost uniform in size, and so is the primary droplet for the three different density ratios. However, by examining the breakup time, it is

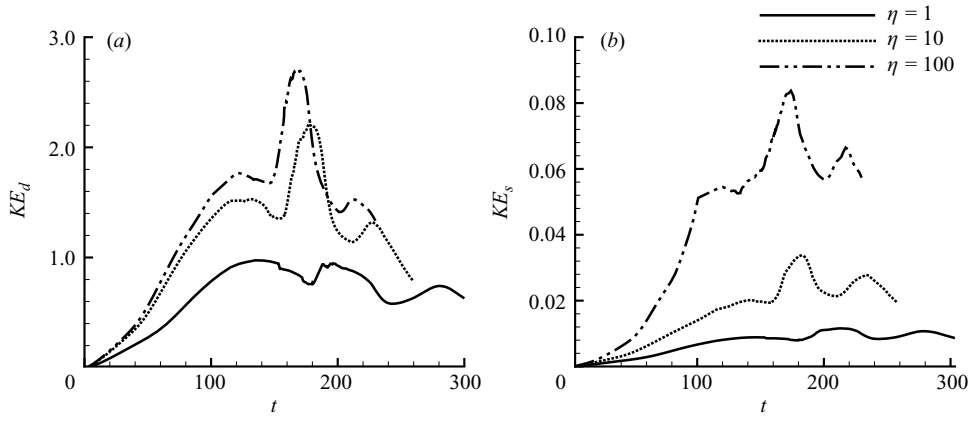

FIGURE 15. Density ratio effect on the kinetic energy per unit mass for both phases. The three cases here are the same cases in figure 14. (*a*) Droplet phase, (*b*) suspending fluid.

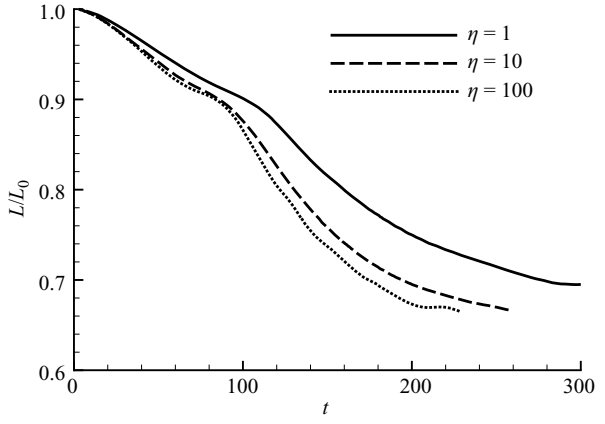

FIGURE 16. Density ratio effect on the evolution of the ligament length. The three cases here are the same cases in figure 14. The length is non-dimensionalized by its initial length.

noted that large density of the suspending fluid tends to retard the breakup, as the pinch-off times for the three density ratios ($\eta = 1$, 10 and 100) are 180.1, 157.0 and 147.7, respectively.

The density ratio effect on the pattern of the relaxation and pinch-off was shown to be small. We shall investigate the effect on evolutions of the kinetic energy and the ligament length. Figure 15 displays kinetic energy per unit mass versus time. The kinetic energy is non-dimensionalized by e_c, and time is non-dimensionalized by t_c. Here, the first trough on the figures indicates the approximate moment when the ligament is pinched off. It can be seen that the relaxation and pinch-off process is retarded by a large density of the suspending fluid. The kinetic energy of the droplet is larger for smaller density of suspending fluid. The difference in the kinetic energy of the suspending fluid is much larger, and this suggests that the lighter the suspending fluid is, the easier it can be moved. In order to compare calculations with different configurations, the reported kinetic energy is per unit mass. If the mass is considered, then the kinetic energy of the whole suspending fluid for the three cases does not vary significantly. The length evolution of the ligament is shown in figure 16, and we

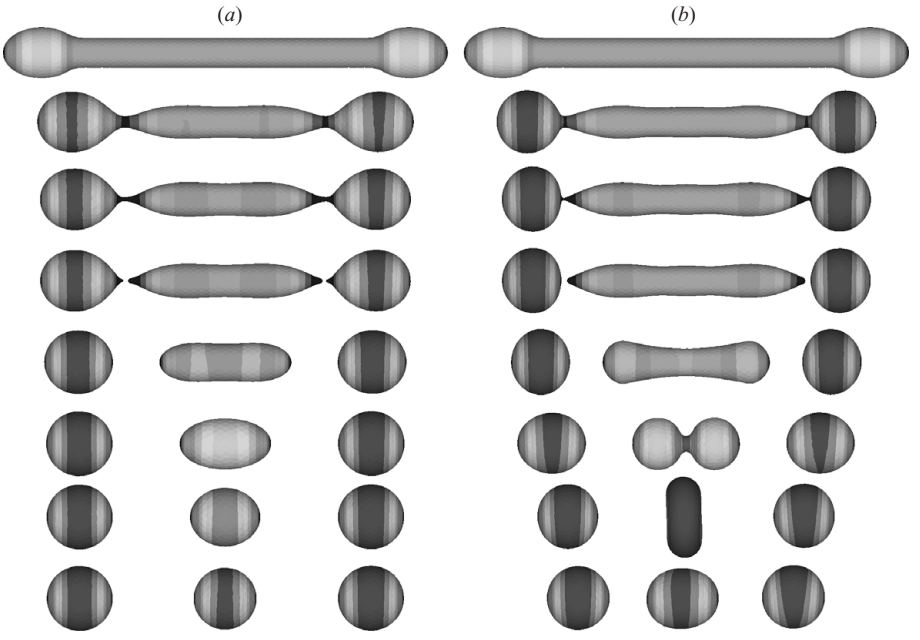

FIGURE 17. The relaxation and breakup process for the elongated droplet with the initial length ratio of 30 and $Oh_d = 3.73 \times 10^{-2}$. The ligaments are shaded by their radius and the contour levels are same as the ones in figure 5. (a) $\eta = 10$; $\lambda = 0.1$; $Oh_s = 1.18$; $t = 0.0$, 345.6, 386.3, 389.1, 468.1, 554.5, 612.1, 670.0. (b) $\eta = 10$; $\lambda = 10$; $Oh_s = 1.18 \times 10^{-2}$; $t = 0.0$, 144.6, 165.0, 165.7, 209.0, 272.4, 369.3, 432.7.

can see that the effect of the density ratio on the length is small. Again, from these two figures, we can conclude that the pattern of the relaxation and breakup for the different density ratios are similar, as the lines in the figures follow a comparable pattern.

4.4. *Length ratio effect*

The effect of the length ratio on the relaxation and breakup process of the initially elongated droplet is examined by carrying out the simulations with $\kappa = 30$ and 15, and by comparing these two length ratios with the length ratio of 20, which was reported in the previous sections. The density and viscosity of the two fluids are fixed for all the simulations. The surface tension coefficient is the same as in the last section. The Ohnesorge number (Oh_d) based on the droplet properties is 3.73×10^{-2}.

4.4.1. *Length ratio of 30*

Figure 17 shows the history of the relaxation and breakup of the ligament with $\kappa = 30$ for two different cases (figures 17a and 17b). These two cases are: (a) $\eta = 10$, $\lambda = 0.1$, $Oh_s = 1.18$; (b) $\eta = 10$, $\lambda = 10$, $Oh_s = 1.18 \times 10^{-2}$. The times are non-dimensionalized by the characteristic time t_c. For case (a), the viscosity ratio is 0.1 which is less than $O(1)$. The filament in the neck region has the shape of a cylinder, which is similar to the shape of the case in figure 5(a) where the viscosity ratio is also 0.1, but with a length ratio of 20. After the two end droplets pinch off, the middle section is also nearly pointed, and this middle section experiences relaxation. Finally, the middle section relaxes to a spherical droplet without any oscillation. For the case in figure 17(b), the necking shape is similar to the cases with a viscosity ratio greater

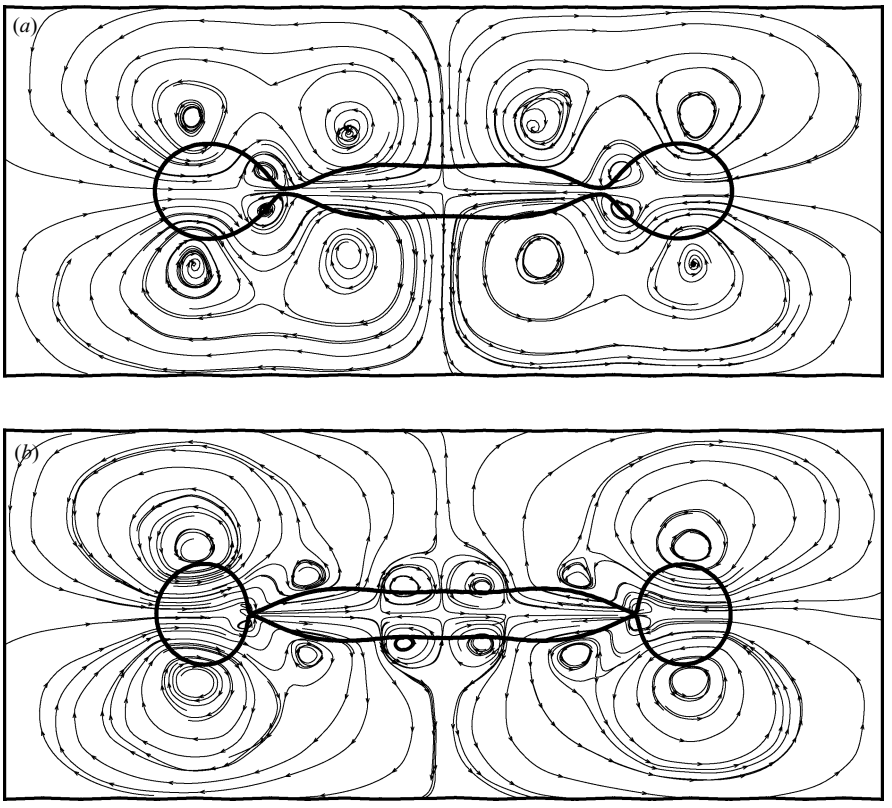

FIGURE 18. The vortex-ring pattern just before the breakup for the droplet with $\kappa = 30$. (a) Stream lines in the x–y plane for case of figure 17(a). (b) Stream lines in the x–y plane for case of figure 17(b). Note that these streamlines are interpolated from three-dimensions and are approximate.

than $O(1)$ in the previous sections. However, the middle section with two pointed ends is a little bit wavy (see figure 17b at $t = 144.6$, 165.0 and 165.7). These waves vanish as time progresses, and two bulbous ends are generated due to the contracting of the two pointed ends (see figure 17b at $t = 209.0$). Then a neck region is created, and because the lateral curvature is larger than the radial curvature, but in the opposite direction, the surface tension forces at this neck region pull the interface outwards. This leads to the reopening of the neck, and the two bulbous ends collapse to a toroid, which then oscillates. It is clear that the created droplet in the middle section for the length ratio of 30 is much larger than the one with length ratio of 20.

The streamlines for the above two cases near the breakup are shown in figure 18. Again vortex rings are observed for both cases, and the total circulation in the whole domain is zero, as the vortex rings are opposite in direction. However, there are only six vortex rings for the case in figure 18(a), while there are 8 vortex rings for the case in figure 18(b). The vortex rings near the centre and at the neck region for the case in figure 18(a) are much larger than the ones for the case in figure 18(b). There are four small vortex rings in the middle section for the case in figure 18(b), and these vortex rings lead to the wavy shape.

A simple explanation of why the vortex rings are larger in size for the small viscosity ratio is given here. Assume that the velocity (or momentum) on the interface caused

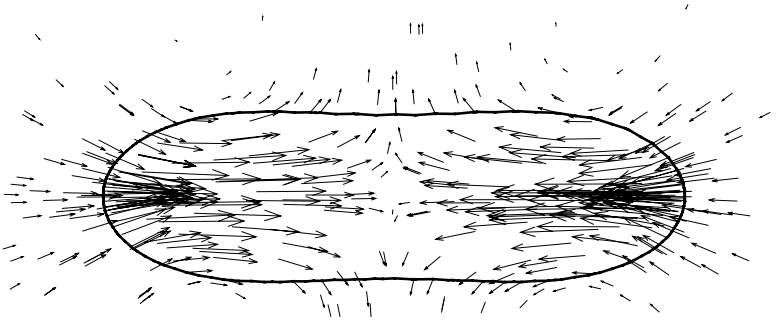

FIGURE 19. Velocity field and the shape of the droplet's middle section at $t = 468.1$ for the case of figure 17(a) in the x–y plane. The velocity vectors are scaled according to their magnitude.

by the surface tension forces is almost same in magnitude, and thus the viscous shear stresses on the interface are the same. Then for a two-dimensional two-phase flow, we have

$$\mu_s \frac{\partial u_i}{\partial x_s} = Constant, \tag{4.2}$$

where u_i is the interface velocity, and x denotes representative length. So for the same constant in (4.2) for different viscosity ratios, it is clear that larger viscosity of the suspending flow needs longer distance (x_s) to diffuse the momentum. By comparing figure 18 with figure 10, it is noted that although the number of the vortex rings are the same for the case with $\lambda = 0.1$, the size of the vortex rings at the middle section for the large length ratio is much greater than that of the length ratio of 20. For cases with $\lambda \gg O(1)$, the number of the vortex rings is much different. There are two more vortex rings in the middle section for the large length ratio.

The relaxation pattern of the middle section after the pinch-off of the two end droplets for the two cases in figure 17 is distinctly different. In order to understand the difference, a detailed examination of the fluid fields is necessary. Figure 19 displays the velocity fields for $\lambda = 0.1$ at $t = 468.1$. The velocities in the centre move the portion of the interface there outwards, and the velocities at the two ends are moving towards the centre. The large surface tension forces at the two ends make the velocity in the centre greater until a spherical shape is reached. Figure 20 shows the velocity fields for the case with $\lambda = 10$ at three different times. There are two large vortex rings near the centre, and these two vortex rings decrease the radius of the neck region ($t = 209.0$). As the two ends move towards the centre, the two inner vortices become stronger, and the necking is accelerated, which increases the lateral curvature at a higher speed than the radial curvature ($t = 257.8$). Later, the lateral curvature becomes larger than the radial curvature, and the surface tension forces move the interface and the fluid in the neck region outwards ($t = 275.1$). The two inner vortex rings break down. Finally, the neck is reopened, and the middle section experiences damped oscillation.

4.4.2. *Length ratio of 15*

Three cases of the relaxation and breakup of an elongated droplet with a length ratio of 15 are reported and discussed in this section. The density ratio for the three cases is 10, and the viscosity ratio for each case is 0.1, 10 and 100, respectively. The history of the shape relaxation of the three cases is displayed in figure 21. There are three droplets after the breakup with a satellite droplet in the middle for the cases with $\lambda = 10$ and 100, while there are only two primary droplets for case with $\lambda = 0.1$.

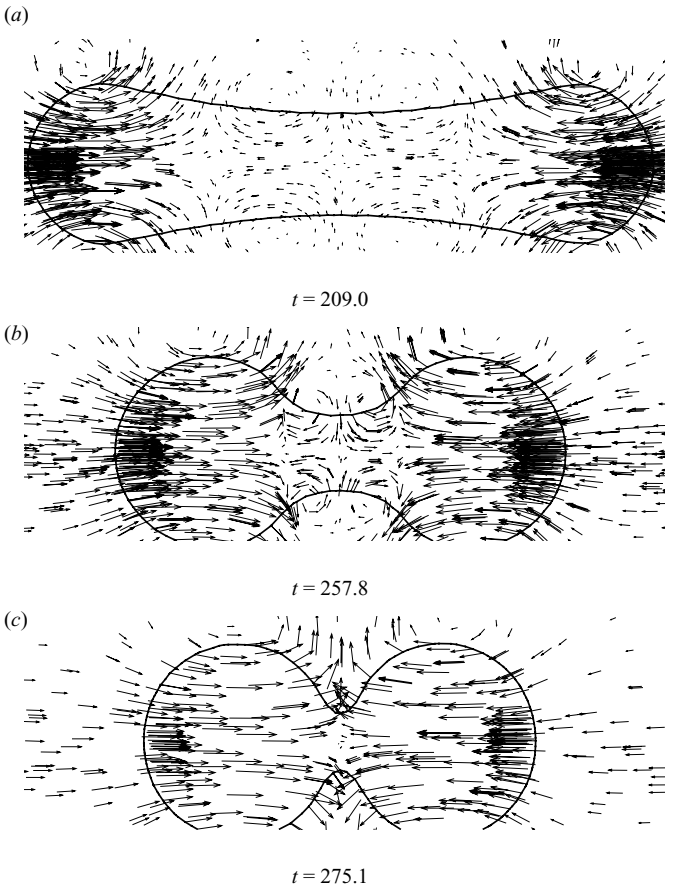

FIGURE 20. History of the relaxation of the middle section after the pinch-off of the two ends droplets for the case in figure 17(*b*) in the x–y plane. The velocity vectors are scaled according to their magnitude.

The shape of the neck region for viscosity ratio of 0.1 is similar to that of the cases with the same viscosity ratio reported in the previous sections. The shape of the neck region for the higher viscosity ratios is also similar to that of the cases with large viscosity ratios that were presented in the previous sections. The differences can be explained by the velocity fields shown in figure 22. For the case with a viscosity ratio of 0.1 (figure 22*a*), the maximum velocity on the interface near the neck region is at the centre of the neck region. This indicates that the neck region with the largest curvature experiences a rapid decrease in radius until pinch-off occurs, and thus only two primary droplets are generated. However, for the viscosity ratio of 10 (figure 22*b*), the largest velocity on the interface near the neck region occurs away from the centre. Thus, the radial dimension of the interface where the end bulb joins the cylindrical part diminishes faster than the radius at the centre. Finally, two neck regions appear near the two ends (figure 21*b* at $t = 136.8$), and a satellite droplet is created (figure 21*b* at $t = 172.9$). Comparing these three cases with the cases discussed in the previous sections, it is clear that the satellite droplet size in the middle section depends strongly on the length ratio.

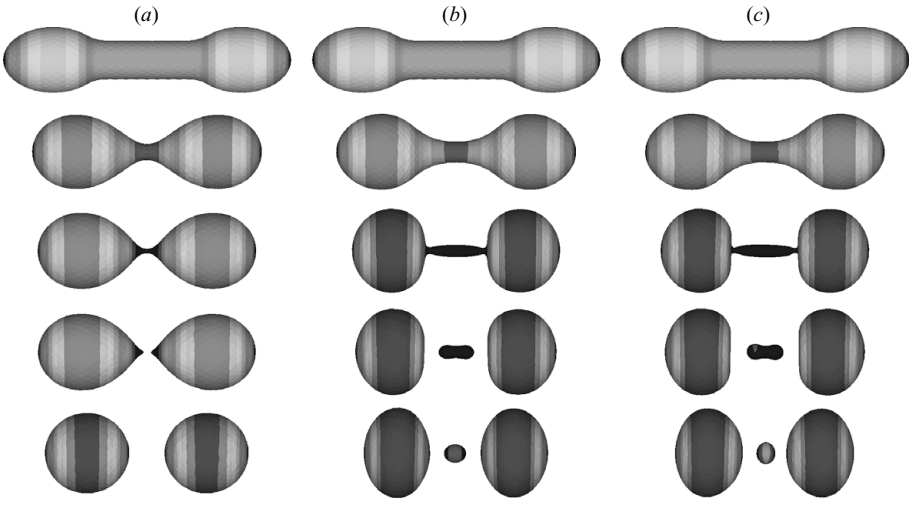

FIGURE 21. The relaxation and breakup process for the elongated droplet with an initial length ratio of 15 and $Oh_d = 3.73 \times 10^{-2}$. (*a*) $\eta = 10$; $\lambda = 0.1$; $Oh_s = 1.18$; $t = 0.0$, 216.0, 266.6, 270.7, 374.6. (*b*) $\eta = 10$; $\lambda = 10$; $Oh_s = 1.18 \times 10^{-2}$; $t = 0.0$, 100.8, 136.8, 145.5, 172.9. (*c*) $\eta = 10$; $\lambda = 100$; $Oh_s = 1.18 \times 10^{-3}$; $t = 0.0$, 100.8, 134.0, 144.1, 187.3.

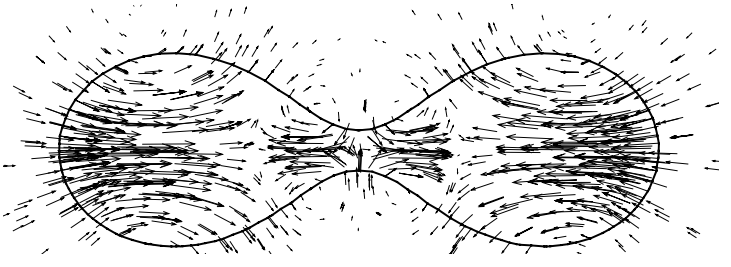

(*a*) $\lambda = 0.1$, $t = 216.0$

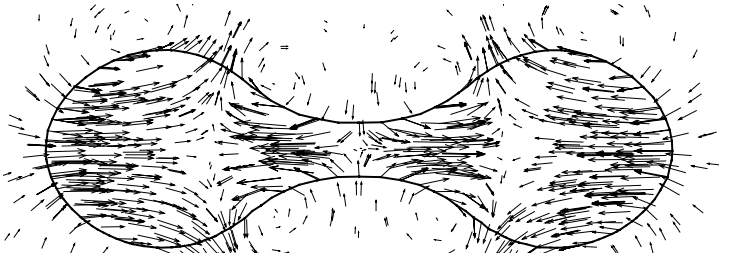

(*b*) $\lambda = 10$, $t = 100.8$

FIGURE 22. Velocity fields for two of the cases in figure 21 in the x–y plane. The velocity vectors are scaled according to their magnitude. However, for clarity, the scales for the two figures are not the same.

4.4.3. *Kinetic energy and evolution of the length*

It has been shown in the previous sections that the length ratio has a significant effect on the evolution of the relaxation and breakup as well as the velocity fields. A quantitative analysis of the effect is performed by comparing the evolution of the

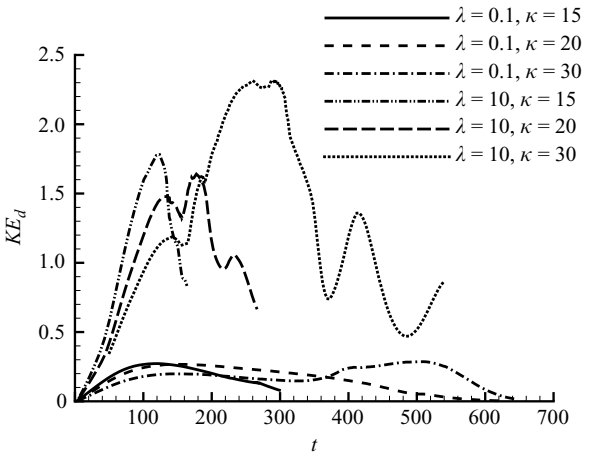

FIGURE 23. Length ratio effects on the kinetic energy per unit mass of the ligament; $\eta = 10$.

kinetic energy and the length of the ligament for the three different length ratios ($\kappa = L_0/r_0$) of 15, 20 and 30. The density ratio for all the cases here is 10.

Figure 23 displays the history of the kinetic energy of the ligament per unit mass. The first peak on the left denotes that the necking process starts to dominate. The fluid flow driven by the highest pressure near the neck region retards the motion of the relaxation, thus the kinetic energy decreases. For the same viscosity ratio, the first peak is larger for the smaller length ratio and also happens earlier. This suggests that for a longer ligament, since more liquid mass must be moved, the motion is retarded because the surface tension forces of the cases are all about the same in the early stages. It is also clear that the kinetic energy for the cases with a viscosity ratio of 10 is much larger than that with a viscosity ratio of 0.1. This indicates that the viscous dissipation for the smaller viscosity ratio is much larger. For the cases with greater viscosity ratio and large length ratio ($\lambda = 10$ and $\kappa = 20$, $\lambda = 10$ and $\kappa = 30$), after the breakup of the end droplets, the middle section experiences relaxation and oscillation. This effect is also evident in the oscillation of the kinetic energy. However, the kinetic energy for $\lambda = 10$ and $\kappa = 15$ decreases monotonically because the middle section is very small compared to the two primary droplets. The gain of the kinetic energy due to the relaxation and oscillation of the middle section is minimal.

Figure 24 shows the length evolution of the ligament for all the cases, where the length is non-dimensionalized by the corresponding initial ligament length (L_0). For the same viscosity ratio, the two ends move faster for smaller length ratios, which is consistent with the length ratio effect on the kinetic energy discussed previously. The evolution of the length follows almost the same pattern for the cases with the same viscosity ratio, i.e. for the smaller viscosity ratio, the length continuously decreases; while the length diminishes faster in the early stage, then slower and then faster for the cases with higher viscosity ratio. However, it is observed that for the length ratio of 30 and the viscosity ratio of 10, the length does not decrease smoothly because of oscillation of the middle section after the breakup of the two primary droplets.

4.5. *Volume of droplets*

To investigate the effects of the length ratio, the viscosity ratio, and the density ratio on the volume of the newly created primary and satellite droplets, a list of the volume for all the cases is shown in table 1. The volume is non-dimensionalized by the volume

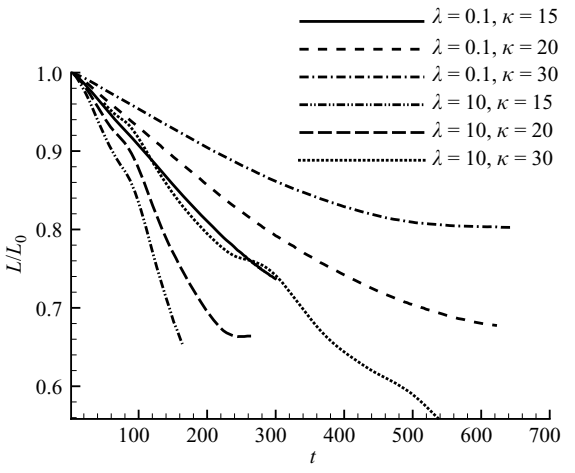

FIGURE 24. Length ratio effects on the evolution of the ligament length; $\eta = 10$.

κ	λ	η	Satellite	Primary left	Primary right
15	0.1	10	0.000	9.390	9.405
15	10	10	0.124	9.271	9.268
15	100	10	0.162	9.213	9.210
20	0.1	10	0.452	11.004	11.013
20	100	1	3.424	9.461	9.456
20	10	10	3.479	9.405	9.393
20	100	10	3.661	9.318	9.308
20	100	100	3.747	9.164	9.184
30	0.1	10	9.059	10.399	10.386
30	10	10	10.392	9.677	9.663

TABLE 1. Volumes of the created primary and satellite drops.

of a sphere with radius of r_0. It can be seen that larger length ratio creates larger satellite drops, and for $\kappa = 30$, the satellite droplets almost have same size as the primary ones. The sizes of the primary drops are nearly equal, since the two ends of all the cases are initially the same. For the same density ratio and length ratio, the satellite droplet becomes larger as the viscosity ratio increases. Large density ratios also tend to create larger satellite droplets. The sizes of the satellite droplets are quite different for viscosity ratios less than unity and larger than unity, due to the distinct necking process. For each case, the volume difference between the two primary drops is as small as 0.15 %. The total volumes of the created drops for cases with the same length ratio are nearly uniform, with a variation of around 1 %. This implies that the numerical method is good in conserving the total mass of each phase.

4.6. *End-pinching mechanism*

The mechanism of the relaxation of a ligament leading to pinch off the two end droplets, and also the formation of satellite droplets, is the end-pinching mechanism proposed by Stone *et al.* (1986) and Stone & Leal (1989), and further was depicted schematically by Qian & Law (1997). However, recently, based on their numerical simulations, Tong & Wang (2007) reported that this end-pinching mechanism was 'flawed' and proposed a correction of the mechanism. As pointed out in the

introduction, the major difference for the problem studied by these two groups is that the viscosity ratio for Tong & Wang (2007) is infinity, while the viscosity ratio for the works by Stone *et al.* (1986) and Stone & Leal (1989) is mainly less than $O(1)$.

Based on our numerical results for different viscosity ratios, by solving the two-phase flow system directly, we have observed two kinds of neck shape. For viscosity ratio less than $O(1)$, a cylinder shape of the necking region is obtained, and in all our simulations the neck breaks up and finally two end droplets are created. The velocities moving towards the centre and the end are symmetric about the neck point. These two velocities induce the reduction of the neck radius. The reduction of the neck radius further increases the pressure in the neck, thus the neck moves inwards. This process is unstable and eventually leads to breakup. This agrees with the theory by Stone *et al.* (1986), Stone & Leal (1989) and Qian & Law (1997). However, for the viscosity ratio greater than $O(1)$, a conical shape of the neck region is observed. Due to the concave curvature in the lateral direction of the neck region, the highest surface tension force occurs away from the place with the smallest radial dimension. The surface tension forces near the neck point may create a net increase or decrease of pressure depending on the magnitude of the lateral curvature. If the surface tension force is driving pressure downwards, then the competition between the flows moves the mass out of the neck region, and the surface tension forces determine the pinch-off or the reopening of the neck region. This agrees with Tong and Wang's analysis (Tong & Wang 2007).

5. Conclusions

The transient motion of the relaxation and pinch-off of an elongated droplet in another viscous fluid has been investigated numerically by a three-dimensional MMIT method. The simulations are in a general regime where both the viscous forces and inertial forces have significant roles, and thus are performed by solving the full Navier–Stokes equations using a finite volume scheme. With an interface of zero thickness, the jump and continuity conditions across the interface are implemented directly without any smoothing. The effects of the viscosity ratio, the density ratio and the length ratio on the process were examined.

Vortex rings were observed for all cases of the relaxation and pinch-off, and these vortex rings play significant roles in the droplet evolution. Vortex rings are created and also collapsed during the process. The pattern of the vortex rings is strongly dependant on the viscosity ratio and the length ratio. For low viscosity ratio ($\lambda \ll O(1)$), the neck region is of the shape of a cylinder, and once this neck region is created and the length of the ligament is long enough, this neck will eventually break up. The velocities in the neck region are symmetric about a plane through the neck point and perpendicular to the relaxation direction. For a large viscosity ratio ($\lambda \gg O(1)$), the neck region is conical, and there is no symmetry for the velocities. This different shape of the neck region confirms the recent observations of the neck shapes for air bubbles in water and water droplets in air by Burton *et al.* (2005). The end-pinching mechanism was also found to be dependent on the viscosity ratio. The mechanism proposed by Stone *et al.* (1986), Stone and Leal (1989) and Qian and Law (1997) is applicable to the smaller viscosity ratio, while the mechanism by Tong and Wang (2007) is suitable for the large viscosity ratio. The motion for the small viscosity ratio is much slower than the one with large viscosity ratio. Capillary waves were observed in the middle section for the length ratio of 30. However, these waves

play no significant roles on the relaxation of the middle section after the breakup of the two end droplets.

The density ratio has minimal effect on the pattern of the relaxation and breakup. However, the motion is retarded by large density of the suspending fluid as more mass must be moved. The length ratio affects the process in a noticeable way. The vortex ring patterns are different for all the three different length ratios. The relaxation and pinch-off process is slowed down by large length ratio as the mass of the droplet is greater. The satellite droplet formation depends strongly on the length ratio.

We thank Professor J. Blair Perot of the University of Massachusetts, Amherst for sharing code in support of this project. The second author thanks the support from the ONR contract N00014-02-1-0507 and the NSF Particulate and Multiphase Processes Program. The authors are grateful to the reviewers for their valuable suggestions.

REFERENCES

Burton, J. C. & Taborek, P. 2008 Bifurcation from bubble to droplet behaviour in inviscid pinch-off. *Phys. Rev. Lett.* **101**, 214502.

Burton, J. C., Waldrep, R. & Taborek, P. 2005 Scaling and instabilities in bubble pinch-off. *Phys. Rev. Lett.* **94** (18), 184502.

Chang, W., Giraldo, F. & Perot, B. 2002 Analysis of an exact fractional step method. *J. Comput. Phys.* **180**, 183–199.

Chen, L., Garimella, S. V., Reizes, J. A. & Leonardi, E. 1999 The development of a bubble rising in a viscous fluid. *J. Fluid Mech.* **387**, 61–96.

Chen, A. U., Notz, P. K. & Basaran, O. A. 2002 Computational and experimental analysis of pinch-off and scaling. *Phys. Rev. Lett.* **88** (17), 174501.

Cohen, I. & Nagel, S. R. 2001 Testing for scaling behaviour dependence on geometrical and fluid parameters in the two fluid drop snap-off problem. *Phys. Fluids* **13**, 3533–3541.

Cresswell, R. W. & Morton, B. R. 1995 Drop-formed vortex rings – the generation of vorticity. *Phys. Fluids* **7**, 1363–1370.

Cristini, V., Blawzdziewicz, J. & Loewenberg, M. 1998 Drop breakup in three-dimensional viscous flows. *Phys. Fluids* **10**, 1781–1783.

Cristini, V., Blawzdziewicz, J. & Loewenberg, M. 2001 An adaptive mesh algorithm for evolving surfaces: simulations of drop breakup and coalesence. *J. Comput. Phys.* **168**, 445–463.

Dai, M. Z. & Schmidt, D. P. 2005 Adaptive tetrahedral meshing in free-surface flow. *J. Comput. Phys.* **208**, 228–252.

Dai, M. Z., Wang, H. S., Perot, J. B. & Schmidt, D. P. 2002 Direct interface tracking of droplet deformation. *Atom. Spray* **12**, 721–735.

Doshi, P., Cohen, I., Zhang, W. W., Siegel, M., Howell, P., Basaran, O. A. & Nagel, S. R. 2003 Persistence of memory in drop breakup: the breakdown of universality. *Science* **302**, 1185–1188.

Eggers, J. 1997 Nonlinear dynamics and breakup of free-surface flows. *Rev. Mod. Phys.* **69**, 865–930.

Ha, J. W. & Leal, L. G. 2001 An experimental study of drop deformation and breakup in extensional flow at high capillary number. *Phys. Fluids* **13**, 1568–1576.

Hua, J. & Lou, J. 2007 Numerical simulation of bubble rising in viscous liquid. *J. Comput. Phys.* **222**, 769–795.

Keim, N. C., Moller, P., Zhang, W. W. & Nagel, S. R. 2006 Breakup of air bubbles in water: memory and breakdown of cylindrical symmetry. *Phys. Rev. Lett.* **97** (14), 144503.

Lamb, H. 1945 *Hydrodynamics*. Dover.

Li, Z. L. & Lai, M. C. 2001 The immersed interface method for the Navier–Stokes equations with singular forces. *J. Comput. Phys.* **171**, 822–842.

Lister, J. R. & Stone, H. A. 1998 Capillary breakup of a viscous thread surrounded by another viscous fluid. *Phys. Fluids* **10**, 2758–2764.

Liu, X. D., Fedkiw, R. P. & Kang, M. J. 2000 A boundary condition capturing method for Poisson's equation on irregular domains. *J. Comput. Phys.* **160**, 151–178.

Lundgren, T. & Koumoutsakos, P. 1999 On the generation of vorticity at a free surface. *J. Fluid Mech.* **382**, 351–366.

Mortazavi, S. & Tryggvason, G. 2000 A numerical study of the motion of drops in Poiseuille flow. Part 1. Lateral migration of one drop. *J. Fluid Mech.* **411**, 325–350.

Papageorgiou, D. T. 1995 On the breakup of viscous-liquid threads. *Phys. Fluids* **7**, 1529–1544.

Perot, B. & Nallapati, R. 2003 A moving unstructured staggered mesh method for the simulation of incompressible free-surface flows. *J. Comput. Phys.* **184**, 192–214.

Peskin, C. S. 1977 Numerical analysis of blood flow in the heart. *J. Comput. Phys.* **25**, 220–252.

Qian, J. & Law, C. K. 1997 Regimes of coalescence and separation in droplet collision. *J. Fluid Mech.* **331**, 59–80.

Quan, S. P. & Hua, J. S. 2008 Numerical studies of bubble necking in viscous liquids. *Phys. Rev.* E **77**, 066303.

Quan, S. P., Lou, J. & Schmidt, D. P. 2009 Modeling merging and breakup in the moving mesh interface tracking method for multiphase flow simulations. *J. Comput. Phys.* **228**, 2660–2675.

Quan, S. P. & Schmidt, D. P. 2006 Direct numerical study of a liquid droplet impulsively accelerated by gaseous flow. *Phys. Fluids* **18**, 102103.

Quan, S. P. & Schmidt, D. P. 2007 A moving mesh interface tracking method for 3D incompressible two-phase flows. *J. Comput. Phys.* **221**, 761–780.

Rallison, J. M. 1984 The deformation of small viscous drops and bubbles in shear flows. *Annu. Rev. Fluid Mech.* **16**, 45–66.

Scardovelli, R. & Zaleski, S. 1999 Direct numerical simulation of free-surface and interfacial flow. *Annu. Rev. Fluid Mech.* **31**, 567–603.

Stone, H. A., Bentley, B. J. & Leal, L. G. 1986 An experimental study of transient effects in the breakup of viscous drops. *J. Fluid Mech.* **173**, 131–158.

Stone, H. A. & Leal, L. G. 1989 Relaxation and breakup of an initially extended drop in an otherwise quiescent fluid. *J. Fluid Mech.* **198**, 399–427.

Sussman, M. & Smereka, P. 1997 Axisymmetric free boundary problems. *J. Fluid Mech.* **341**, 269–294.

Sussman, M., Smereka, P. & Osher, S. 1994 A level set approach for computing solutions to incompressible 2-phase flow. *J. Comput. Phys.* **114**, 146–159.

Taylor, G. I. 1932 The viscosity of a fluid containing small drops of another fluid. *Proc. R. Soc. Lond.* A **138**, 41–48.

Taylor, G. I. 1934 The formation of emulsions in definable fields of flow. *Proc. R. Soc. Lond.* A **146**, 501–523.

Thoroddsen, S. T., Etoh, T. G. & Takehara, K. 2007 Experiments on bubble pinch-off. *Phys. Fluids* **19**, 042101.

Tong, A. Y. & Wang, Z. Y. 2007 Relaxation dynamics of a free elongated liquid ligament. *Phys. Fluids* **19**, 092101.

Unverdi, S. O. & Tryggvason, G. 1992 A front tracking method for viscous, incompressible, multi-fluid flows. *J. Comput. Phys.* **100**, 25–37.

Wu, J. Z. 1995 A theory of three-dimensional interfacial vorticity dynamics. *Phys. Fluids* **7**, 2375–2395.

Zhang, W. W. & Lister, J. R. 1999 Similarity solutions for capillary pinch-off in fluids of differing viscosity. *Phys. Rev. Lett.* **83** (6), 1151–1154.

Zhang, X., Schmidt, D. & Perot, B. 2002 Accuracy and conservation properties of a three-dimensional unstructured staggered mesh scheme for fluid dynamics. *J. Comput. Phys.* **175**, 764–791.

Zheng, X. M., Lowengrub, J., Anderson, A. & Cristini, V. 2005 Adaptive unstructured volume remeshing – II: application to two- and three-dimensional level-set simulations of multiphase flow. *J. Comput. Phys.* **208**, 626–650.

Zhou, H. & Pozrikidis, C. 1993 The flow of ordered and random suspensions of 2-dimensional drops in a channel. *J. Fluid Mech.* **255**, 103–127.